



HAL
open science

Wavelength selection in the twist buckling of pre-strained elastic ribbons

Arun Kumar, Basile Audoly

► **To cite this version:**

Arun Kumar, Basile Audoly. Wavelength selection in the twist buckling of pre-strained elastic ribbons. 2024. hal-04670707v2

HAL Id: hal-04670707

<https://hal.science/hal-04670707v2>

Preprint submitted on 9 Dec 2024

HAL is a multi-disciplinary open access archive for the deposit and dissemination of scientific research documents, whether they are published or not. The documents may come from teaching and research institutions in France or abroad, or from public or private research centers.

L'archive ouverte pluridisciplinaire **HAL**, est destinée au dépôt et à la diffusion de documents scientifiques de niveau recherche, publiés ou non, émanant des établissements d'enseignement et de recherche français ou étrangers, des laboratoires publics ou privés.



Distributed under a Creative Commons Attribution - NonCommercial 4.0 International License

Wavelength selection in the twist buckling of pre-strained elastic ribbons

ARUN KUMAR

Laboratoire de Mécanique des Solides,
CNRS, Institut Polytechnique de Paris, France

BASILE AUDOLY

Laboratoire de Mécanique des Solides,
CNRS, Institut Polytechnique de Paris, France

A competition between short- and long-wavelength twist buckling instabilities has been reported in experiments on thin elastic ribbons having pre-strain concentrated in a rectangular region surrounding the axis. The wavelength of the twisting mode has been reported to either scale (i) as the *width* of the ribbon when the pre-strain is large (short-wavelength case) or (ii) as the *length* of the ribbon when the pre-strain is small (large-wavelength case). Existing one-dimensional rod or ribbon models can only account for large-wavelength buckling. We derive a novel one-dimensional model that accounts for short-wavelength buckling as well. It is derived from non-linear shell theory by dimension reduction and captures in an asymptotically correct way both the non-convex dependence of the strain energy on the twisting strain τ (which causes buckling) and its dependence on the strain *gradient* τ' . The competition between short- and long-wavelength buckling is shown to be governed by the sign of the incremental elastic modulus B_0 associated with the twist gradient τ' . The one-dimensional model reproduces the main features of equilibrium configurations generated in earlier work using 3D finite-element simulations. In passing, we introduce a novel truncation strategy applicable to higher-order dimension reduction that preserves the positiveness of the strain energy even when the gradient modulus is negative, $B_0 < 0$.

Keywords Elastic buckling, Asymptotic dimension reduction, Strain-gradient elasticity.

1. INTRODUCTION

Short-wavelength buckling driven by spatially inhomogeneous pre-strain is ubiquitous in natural phenomena and engineering applications. The edges of maize leaves undulate due to differential growth across their width [HWQ+18]; gut tube forms loops and perversions due to a difference in strain in the tube and in the mesenteric sheet attached to it [SKS+11]; octopuses change their texture and color by tuning the difference in strain in the outer skin and in the underlying layers [Bak22]; and the formation of human fingerprints is driven by differential strain in the skin layers [KN05]. A classical engineering example exhibiting short-wavelength buckling is the wrinkling of a pre-strained layer on an elastic foundation, where the buckling wavelength scales with the *thickness* of the layer, rather than the size of the structure [All69]. There is a large body of work on this problem in the literature [BBE+98; CH11; LHS+14; HLK+12].

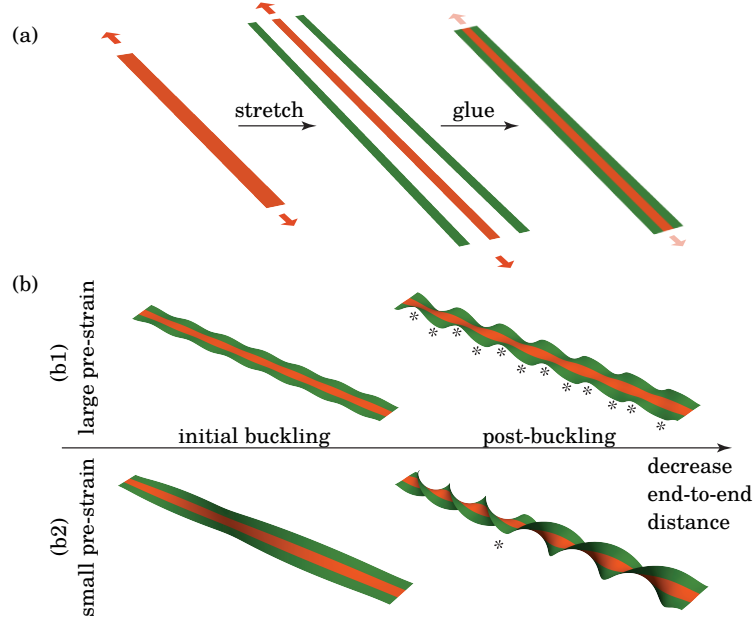


Figure 1.1. Summary of the experiments [GRA23] on thin elastic ribbons with non-uniform pre-strain, exhibiting a competition between short- and long-wavelength instabilities. (a) Preparation of the pre-strained ribbons (see also Figure 2.1 for details): the main parameters are the amount p of extensional pre-strain in the central region (red) and the ratio r of the width of the central region relative to the overall width. (b) Two kinds of instabilities can be observed when the end-to-end distance is decreased: (b1) short-wavelength instability leading to a large number of perversions (star symbols) or (b2) long-wavelength instability leading to a single perversion in the middle.

In this paper, we are interested in structures that exhibit both short- and long-wavelength buckling. By tuning the geometry and the level of pre-strain in a multilayer structure, one can indeed make the two types of modes compete. This has been known for a long time in the context of structural sandwich panels; see the discussion in Section 8.2 of the book by Allen [All69]. By gluing together two elastomeric strips, one of which is pre-stretched, the authors of [HLK+12; LHS+14] have designed a bi-strip in which the competition between short- and long-wavelength instabilities is particularly easy to demonstrate. The endpoints of the bi-strip are initially pulled apart, and when the pulling force is decreased, the bi-strip buckles into a curly pattern whose wavelength scales either as the ribbon length (long-wavelength buckling) or as the ribbon width (short-wavelength case). The transition between long- and short-wavelength is governed mainly by the amount p of the initial pre-stretch and has been characterized experimentally and using finite-element simulations in [LHS+14].

Here, we analyze a variant of the bi-strip, shown in Figure 1.1, that has been introduced in a recent paper [GRA23]. It is made up of *three* ribbons arranged *symmetrically* and glued together, see Figure 1.1(a). The initial pre-stretch is limited to the central strip shown in red in the figure. The behavior of this symmetric strip is similar to that of the original bi-strip and, in particular, it exhibits a competition between short- and long-wavelength buckling governed by the magnitude p of pre-strain, see Figure 1.1(b). Yet, the symmetric ribbon is much easier to analyze as it buckles into a pure-twist mode, see Figure 1.1(b).

In this paper, we derive a *one-dimensional model* for the twist-buckling of pre-strained ribbons and use it as a basis to analyze both the wavelength selection problem and the nonlinear features of buckling. The wavelength selection in the buckling of pre-strained ribbons has been approached in previous work [LA17] using both a rectangular-shell model and a 3D finite-elasticity model for a rectangular block: a linear bifurcation analysis has been set up assuming infinite length, and the long- to short-wavelength transition has been interpreted as a bifurcation on the first critical wavenumber q_c , with $q_c=0$ in the long-wavelength case and $q_c>0$ in the short-wavelength case. As we will see, the one-dimensional model derived in the present paper generates this linear bifurcation analysis more easily and more clearly and exposes the non-linear features of buckling.

Deriving a one-dimensional model for pre-strained ribbons raises the following challenges:

- Dimension reduction for elastic rods or ribbons is most often approached using *linear elasticity*. In the linear setting, the pre-strain enters the one-dimensional model in the form of an effective natural curvature and an effective natural helicity. Both of them happen to be zero for the symmetric distribution of pre-strain used in Figure 1.1, showing that linear elasticity is inapplicable here.
- Non-linear dimension reduction has been used in recent work [GRA23] to derive a one-dimensional energy functional for a twisted ribbon of the form

$$\Phi^* = \int_0^\ell \frac{1}{2} A(\tau(S)) \, dS, \quad (1.1)$$

where $\tau(S)$ is the local twisting strain and $A(\tau)$ is a function generated by the dimension reduction procedure. The main result of the present paper is that the competition between short- and long-wavelength buckling arises from the dependence of the energy on the *gradient* of twisting strain $\tau'(S)$, which is neglected in (1.1).

To tackle these difficulties, we carry out dimension reduction based on a method developed in our group [LA20b], which works in the framework of non-linear elasticity. It captures the effect of the strain gradient $\tau'(S)$ by pushing dimension reduction to *second-order* in the small aspect-ratio parameter. The asymptotic dimension reduction method has already been applied to thin elastic strips and tape springs [AN21; KAL23], and we extend it (i) by including pre-strain and (ii) by proposing a novel truncation strategy for the gradient terms, described in Section 2.5 and 3.3.

The change in the truncation strategy was prompted by the fact that the one-dimensional energy functionals produced by the original version of our dimension reduction method [LA20b; AN21; KAL23] lack an essential smoothness property. We realized this when we first tried generating the results shown in the present paper using the original version of the method [LA20b; AN21; KAL23]: some of the computed solutions had strain energy lower than the stress-free configuration shown in Figure 2.1a, which is paradoxical. In addition, we faced convergence issues in the calculation of the nonlinear equilibria. We had never attempted to solve any equilibrium problem generated by the higher-order dimensional reduction method before, and we believe that *all* the one-dimensional energies that it can generate suffer the same flaw. We expect that the simple fix proposed in the present paper will be applicable to all of them.

In addition to non-trivial wavelength selection, an interesting feature of twist buckling in pre-strained ribbons is their tendency to form uniform helices separated by highly localized features called ‘perversions’ [DH05], where helicity changes sign rapidly—perversions are marked using the star symbols in the post-buckled shapes sketched in Figure 1.1(b). This localization phenomenon takes place in the post-buckled regime and is highly reminiscent of interfaces between phases encountered in phase transformations. It has been characterized experimentally and using finite-element simulations [HLK+12; LHS+14; GRA23]. The analogy with phase transformations has been developed in [GRA23], where a one-dimensional model of the form (1.1) has been derived, including an explicit form of the non-convex potential $A(\tau)$ that predicts the coexistence of helical domains with opposite chiralities. In this paper, we extend this one-dimensional model to include the gradient effect. The gradient term regularizes the non-convex potential $A(\tau)$ and makes it possible to predict how many perversions appear and they form and further evolve on decreasing the separation between the ribbon ends.

Our main contributions are as follows:

- In Section 2, we derive a one-dimensional ribbon model starting from a non-linear shell model. The model is asymptotically exact to second order in the aspect-ratio parameter $\gamma \ll 1$ introduced in (2.3), and captures the dependence of the energy on the gradient of twisting strain (gradient effect).
- Using a linear bifurcation analysis, we show in Section 4 that the competition between short- and long-wavelength instabilities is governed by the sign of the elastic gradient modulus B_0 given in Equation (2.29). We obtain a complete phase diagram for twist buckling in Figure 4.2, predicting the nature of first buckling mode in terms of reduced parameters. The diagram is fully consistent with earlier experimental and finite-element results.
- In Section 4.4, a weakly non-linear analysis of the long-wavelength case is proposed, showing how the incipient sinusoidal mode localizes into a two-phase solution having a sharp interface. Specifically, the length of the interface separating two phases is shown to scale as the inverse square root of the imposed end-to-end shortening minus the critical end-to-end shortening.
- In Section 5, the post-buckling behavior is investigated. The one-dimensional model captures the fast localization of the quasi-sinusoidal initial buckling mode into coexisting phases having almost uniform twist strain $\tau(S)$ each, with alternating signs. The gradient term also helps to resolve the thin interfaces between these phases, called perversions, where the twist strain varies quickly. The analysis of these interfaces uses a non-convex functional regularized by the gradient effect, in close analogy with our earlier work on phase separation in elasto-capillary rods [LA20a] and on propagating instabilities in cylindrical balloons [LA18].
- The one-dimensional model is derived by dimension reduction with the help of the symbolic calculation language Wolfram Mathematica [22]. All supporting files are publicly available [KA24] and could serve as a basis for similar derivations in the future. We also distribute the source files that generate the equilibrium solutions using the open-source solver for ordinary differential equations Auto-07p [KA24].

2. DERIVATION OF THE ONE-DIMENSIONAL RIBBON MODEL

In this section, a one-dimensional energy functional describing a thin ribbon undergoing combined stretching and twisting is derived in the form

$$\Phi^* = \int_0^\ell W(p, r, \varepsilon; \tau(S), \tau'(S), \tau''(S)) \, dS + [W_b(p, r; \tau(S), \tau'(S))]_0^\ell. \quad (2.1)$$

The following dimensionless quantities are used: ℓ is the ribbon length, p is the extensional pre-strain embedded in the central part of the ribbon, r is the ratio of the widths of this central part to the width of the full ribbon, ε is the average longitudinal strain imposed by the clamps at both ends of the ribbon, S is the length coordinate and τ is the twisting strain. In terms of these quantities, we derive a strain energy W per unit length and a boundary contribution $[W_b]_0^\ell = W_b(\ell) - W_b(0)$. The functions $W(p, r, \varepsilon; \tau, \tau', \tau'')$ and $W_b(p, r; \tau, \tau')$ are defined in Subsection 2.6.

The procedure for deriving the energy is adapted from our earlier work on higher-order dimension reduction for non-linear elastic rods [LA20b] and tape springs [KAL23], see in particular Appendix B in [KAL23]. Details of the dimension reduction procedure can be found in the Supplementary Material [KA24] and we outline the key steps below.

Central to the derivation procedure is the assumption of scale separation,

$$\tau^{(k)}(S) = \mathcal{O}(\gamma^k), \quad (2.2)$$

which states that the successive derivatives of the twisting strain $\tau^{(k)} = \frac{d^k \tau}{dS^k}$ scale as the k -th power, γ^k , of the scale separation parameter

$$\gamma := \frac{a}{L} \ll 1. \quad (2.3)$$

Here, a is the ribbon width and L is the ribbon length, in physical variables.

The dimension reduction is based on a shell model we describe in Subsection 2.2. The procedure entails calculating the optimal values of the cross-sectional displacements in terms of the one-dimensional twist strain $\tau(S)$ and its derivatives, by solving a hierarchy of elasticity problems in the cross-section. The optimal cross-sectional displacements furnish an approximation of the membrane and bending strain to order γ^2 , which are inserted into the strain energy of the shell model. Carrying out a partial integration with respect to the transverse coordinate, we derive the strain energy in the form of a one-dimensional functional of the twist strain distribution $\tau(S)$. These steps are detailed in the upcoming subsections.

2.1. Geometry

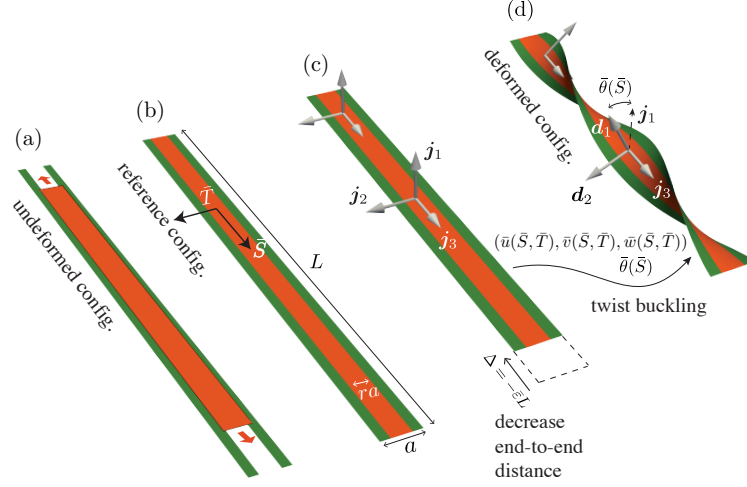


Figure 2.1. Configurations of the ribbon: starting from (a) the relaxed state, (b) the ribbon is fabricated by stretching the central part (in red) and then gluing it to the two symmetric flanks (in green) in their relaxed state. Next, (c) the end-to-end distance is decreased by $\Delta = -\bar{\epsilon}L$, where $\bar{\epsilon}$ is the average imposed strain along the axis. Due to the pre-strain, the planar configuration (c) is not always stable and (d) the ribbon may undergo twist buckling.

We start by recalling the main steps of the experimental procedure used in [GRA23]. The ribbon is fabricated by assembling the three thin ribbons shown in their relaxed states in Figure 2.1a. The middle part is stretched with extensional strain denoted as $\bar{p} > 0$. By Poisson's effect, it contracts transversally—note that the central region in red initially overlaps the green flanks in Figure 2.1(a) and this overlap disappears after pre-stretching in Figure 2.1(b). The resulting ribbon is then glued to the two green ribbons along their long edges. In this experiment, the gluing is achieved by reticulating the green polymer in a mould containing the pre-stretched central part, see [GRA23] for details. By design, the glued/molded green parts have the same thickness as the red middle part in the configuration shown in Figure 2.1(b). We refer to the configuration Figure 2.1(b) as the *reference configuration*, and denote respectively by $\bar{S} \in (0, L)$ and $\bar{T} \in (-a/2, +a/2)$ the arc-length and the transverse coordinate in this reference configuration. The pre-strain in this reference state is described by the function

$$\bar{\epsilon}_p(\bar{T}) = \begin{cases} \bar{p} & \text{if } |\bar{T}| \leq \frac{ra}{2} \\ 0 & \text{if } \frac{ra}{2} \leq |\bar{T}| \leq \frac{a}{2} \end{cases}, \quad (2.4)$$

where a is the width of the composite ribbon, ra is the width of the central part, and a is the width ratio.

Next, the terminal cross-sections of the ribbon at $\bar{S} = 0$ and $\bar{S} = L$ are clamped: both the displacement and rotation of the terminal cross-sections are restrained. The clamps are next moved towards one another and we denote by Δ the end-to-end shortening, see Figure 2.1(c). Depending on the end-to-end shortening Δ , on the amount of the pre-strain \bar{p} and on the geometrical and mechanical properties of the ribbon, the planar ribbon configuration may buckle into the twisted configuration shown in Figure 2.1d.

2.2. Shell model

In the experiments, the thickness-to-width ratio is small, of the order $t/a \sim 1/10$. We will therefore use a thin shell model as the starting point of the dimension reduction method. The thin shell model is presented in the remainder of this section.

2.2.1. Shell kinematics

In our previous work on thin ribbons [AN21; KAL23], we introduced a parameterization of the ribbon mid-surface $(\bar{S}, \bar{T}) \mapsto \bar{\mathbf{x}}(\bar{S}, \bar{T})$ in the form

$$\bar{\mathbf{x}}(\bar{S}, \bar{T}) = \bar{\mathbf{y}}(\bar{S}) + \bar{w}(\bar{S}, \bar{T}) \mathbf{d}_1(\bar{S}) + (\bar{T} + \bar{u}(\bar{S}, \bar{T})) \mathbf{d}_2(\bar{S}) + \bar{v}(\bar{S}, \bar{T}) \mathbf{d}_3(\bar{S}). \quad (2.5)$$

In the right-hand side, we use the centerline position $\bar{\mathbf{y}}(\bar{S})$, the orthonormal frame of directors $(\mathbf{d}_1(\bar{S}), \mathbf{d}_2(\bar{S}), \mathbf{d}_3(\bar{S}))$ and the cross-sectional displacements $(\bar{w}, \bar{v}, \bar{u})$ along these directors. The centerline position $\bar{\mathbf{y}}(\bar{S})$ and the directors $\mathbf{d}_i(\bar{S})$ are functions of the longitudinal arc-length \bar{S} only. By contrast, the cross-sectional displacements depend on the transverse coordinate \bar{T} as well. The parameterization in (2.5) uses two sets of unknowns that are well suited to dimension reduction: on the one hand, the variables $\bar{\mathbf{y}}(\bar{S})$ and $\mathbf{d}_i(\bar{S})$ are defined at the centerline and will be retained in the one-dimensional model; on the other hand, the cross-sectional displacements $(\bar{w}(\bar{S}, \bar{T}), \bar{v}(\bar{S}, \bar{T}), \bar{u}(\bar{S}, \bar{T}))$ will be eliminated.

In classical rod theories, the centerline $\bar{\mathbf{y}}(\bar{S})$ and the directors $\mathbf{d}_i(\bar{S})$ are associated with the following one-dimensional strain: axial strain $\bar{\varepsilon}(\bar{S})$, bending strains $\bar{\kappa}_1(\bar{S})$ and $\bar{\kappa}_2(\bar{S})$ and twisting strain $\bar{\tau}(\bar{S})$. In the present work, we limit attention to a typical ribbon configuration shown in Figure 2.1(d), such that:

1. the centerline remains straight,
2. and the axial strain $\bar{\varepsilon}(\bar{S})$ is uniform.

With the first assumption, we limit attention to *twist buckling* and ignore the *Euler buckling* modes reported in [GRA23] which involve bending and occur when the pre-strain is small. However, we will still be able to discuss the *onset* of Euler buckling based on the sign of the internal force, see Equation (3.3) and Figure 4.2.

The second assumption is an approximation that cannot be justified rigorously. It simplifies the one-dimensional model significantly by condensing out the unknown longitudinal displacement into a *single*, global degree of freedom $\bar{\varepsilon}$. This simplification captures the nonlinear coupling at the heart of twist buckling, whereby axial strain influences the twisting behavior, ignoring how twist buckling affects stretching in return.

Both these assumptions could be relaxed at the price of increased mathematical complexity, see the analysis in our previous work [KAL23].

These assumptions have the following consequences:

- The centerline is given by $\bar{\mathbf{y}}(\bar{S}) = (1 + \bar{\varepsilon}) \bar{S} \mathbf{j}_3$, where the *uniform* axial strain $\bar{\varepsilon}$ is defined as

$$\bar{\varepsilon} = -\frac{\Delta}{L}, \quad (2.6)$$

in terms of the end-to-end displacement Δ . When the ends are brought closer to one another, the end-to-end displacement $\Delta > 0$ is counted *positive* and the imposed axial strain $\bar{\varepsilon} < 0$ is counted *negative*.

- At every point \bar{S} along the centerline, the frame of directors rotates about the axis \mathbf{j}_3 of the ribbon. Denoting the angle of rotation of the cross-sections as $\bar{\theta}(\bar{S})$, we have

$$\begin{aligned} \mathbf{d}_1(\bar{S}) &= \cos \bar{\theta}(\bar{S}) \mathbf{j}_1 + \sin \bar{\theta}(\bar{S}) \mathbf{j}_2 \\ \mathbf{d}_2(\bar{S}) &= -\sin \bar{\theta}(\bar{S}) \mathbf{j}_1 + \cos \bar{\theta}(\bar{S}) \mathbf{j}_2 \\ \mathbf{d}_3(\bar{S}) &= \mathbf{j}_3. \end{aligned} \quad (2.7)$$

- The one-dimensional bending strains along the length and width of the ribbon are identically zero: $\bar{\kappa}_1(\bar{S}) = \bar{\kappa}_2(\bar{S}) = 0$. The one-dimensional model will therefore be a functional of the twisting strain distribution $\bar{\tau}(\bar{S})$, depending on the parameter $\bar{\varepsilon}$ (uniform axial strain) as well.

In view of this, the parameterization of the ribbon mid-surface in (2.5) can be simplified as

$$\bar{\mathbf{x}}(\bar{S}, \bar{T}) = (1 + \bar{\varepsilon}) \bar{S} \mathbf{j}_3 + \bar{w}(\bar{S}, \bar{T}) \mathbf{d}_1(\bar{S}) + (\bar{T} + \bar{u}(\bar{S}, \bar{T})) \mathbf{d}_2(\bar{S}) + \bar{v}(\bar{S}, \bar{T}) \mathbf{j}_3, \quad (2.8)$$

where the first term on right-hand side in (2.8) is the centerline position and remaining terms capture the cross-sectional deformation associated with twisting, including the classical warping effect at leading order.

To warrant the uniqueness of the above parameterization, we enforce the kinematic constraints

$$\int_{-\frac{a}{2}}^{+\frac{a}{2}} (\bar{u}(\bar{S}, \bar{T}), \bar{v}(\bar{S}, \bar{T}), \bar{w}(\bar{S}, \bar{T})) d\bar{T} = \mathbf{0} \quad \text{and} \quad \int_{-\frac{a}{2}}^{+\frac{a}{2}} \bar{T} \bar{w}(\bar{S}, \bar{T}) d\bar{T} = 0, \quad (2.9)$$

as in our earlier work on dimension reduction for thin elastic rods [LA17] and tape springs [KAL23]. The first equality warrants that the centerline $\bar{\mathbf{y}}(\bar{S})$ is the centroid of the cross-section labelled by \bar{S} , i.e., $\bar{\mathbf{y}}(\bar{S}) = \frac{1}{a} \int_{-\frac{a}{2}}^{+\frac{a}{2}} \bar{\mathbf{x}}(\bar{S}, \bar{T}) d\bar{T}$. The second condition warrants that the angle $\bar{\theta}(\bar{S})$ is the average rotation of the cross-section about \mathbf{j}_3 , as discussed in Section-2(a) of [KAL23].

We further assume that the relative rotation of any couple of tangent planes distant by at most the ribbon width is moderate, so we can use *locally* the von Kármán approximation in the local frame of directors. The von Kármán approximation yields *weakly non-linear* expressions for the membrane strains in terms of the cross-sectional displacements $(\bar{w}, \bar{v}, \bar{u})$,

$$\begin{aligned} \bar{E}_{SS}(\bar{S}, \bar{T}) &= \bar{\varepsilon} + \bar{\varepsilon}_p(\bar{T}) + \bar{v}_{,\bar{S}}(\bar{S}, \bar{T}) + \frac{1}{2} (-\bar{T} \bar{\tau}(\bar{S}) + \bar{w}_{,\bar{S}}(\bar{S}, \bar{T}))^2, \\ \bar{E}_{TT}(\bar{S}, \bar{T}) &= -\nu (\bar{\varepsilon} + \bar{\varepsilon}_p(\bar{T})) + \bar{u}_{,\bar{T}}(\bar{S}, \bar{T}) + \frac{1}{2} \bar{w}_{,\bar{T}}^2(\bar{S}, \bar{T}), \\ \bar{E}_{ST}(\bar{S}, \bar{T}) &= \frac{1}{2} (\bar{\tau}(\bar{S}) (\bar{w}(\bar{S}, \bar{T}) - \bar{T} \bar{w}_{,\bar{T}}(\bar{S}, \bar{T})) + \bar{v}_{,\bar{T}}(\bar{S}, \bar{T}) + \bar{u}_{,\bar{S}}(\bar{S}, \bar{T}) + \bar{w}_{,\bar{S}}(\bar{S}, \bar{T}) \bar{w}_{,\bar{T}}(\bar{S}, \bar{T})). \end{aligned} \quad (2.10)$$

The strain $\bar{E}_{ij}(\bar{S}, \bar{T})$ characterize the change in lengths measured along the mid-surface, between the undeformed configuration in Figure 2.1(a) and the buckling configuration in Figure 2.1(d). In the right-hand side of (2.10), commas in subscript denote a partial derivative with respect to the mid-surface coordinate listed next, and $\bar{\tau}(\bar{S})$ is the twist rate,

$$\bar{\tau}(\bar{S}) = \bar{\theta}'(\bar{S}). \quad (2.11)$$

Primes denote differentiation of the functions depending solely on the arc-length variable \bar{S} , such as $\bar{\theta}(\bar{S})$, i.e., $\bar{\theta}' = d\bar{\theta}/d\bar{S}$. The expressions of the membrane strain in (2.10) are similar to that obtained in [KAL23], except for the presence of the pre-strain $\bar{\varepsilon} + \bar{\varepsilon}_p(\bar{T})$ that captures the transformation from the undeformed configuration in Figure 2.1(a) to the planar solution in Figure 2.1(c). The strain expression in (2.10) can be justified by exactly the same argument as in our previous work [KAL23], which shows that they are asymptotically exact within the same scaling assumptions as the von Kármán approximation.

The bending strains is obtained similarly, and the result is exactly identical to that obtained in [KAL23],

$$\begin{aligned}\bar{B}_{SS}(\bar{S}, \bar{T}) &= -\bar{\tau}'(\bar{S}) \bar{T} + \bar{w}_{,\bar{S}\bar{S}}(\bar{S}, \bar{T}), \\ \bar{B}_{TT}(\bar{S}, \bar{T}) &= \bar{w}_{,\bar{T}\bar{T}}(\bar{S}, \bar{T}), \\ \bar{B}_{ST}(\bar{S}, \bar{T}) &= -\bar{\tau}(\bar{S}) + \bar{w}_{,\bar{S}\bar{T}}(\bar{S}, \bar{T}).\end{aligned}\tag{2.12}$$

2.2.2. Nondimensionalization

To simplify the forthcoming calculations, we use the following set of *non-dimensional* variables, which bear no overbars in our notation:

$$\begin{aligned}S &= \frac{\bar{S}}{a}, & u &= \frac{\bar{u}}{a(a k)^2}, & \theta &= \frac{\bar{\theta}}{a k}, & E_{\alpha\beta} &= \frac{\bar{E}_{\alpha\beta}}{(a k)^2}, \\ T &= \frac{\bar{T}}{a}, & v &= \frac{\bar{v}}{a(a k)^2}, & \tau &= \frac{\bar{\tau}}{k}, & B_{\alpha\beta} &= \frac{\bar{B}_{\alpha\beta}}{k}, \\ k &= \frac{1}{\sqrt{12(1-\nu^2)}} \frac{t}{a^2}, & w &= \frac{\bar{w}}{a^2 k}, & \varepsilon &= \frac{\bar{\varepsilon}}{(a k)^2}, & p &= \frac{\bar{p}}{(a k)^2},\end{aligned}\tag{2.13}$$

where t is the ribbon thickness. The twisting strain $\bar{\tau}$ has been rescaled using a typical inverse length $k \sim t/a^2$ relevant to thin ribbons, which has been shown in previous work [AN21] to govern the transition from a Kirchhoff-rod-like linear response ($\bar{\tau} \ll k$, $\tau \ll 1$) to an inextensible, essentially nonlinear response ($\bar{\tau} \gg k$, $\tau \gg 1$). When expressed in terms of the dimensionless variables, the energy will no longer explicitly depend on the width a or thickness t of the ribbon.

In terms of the scaled rotation $\theta(S)$, the twisting strain in (2.11) takes the form

$$\tau(S) = \theta'(S),\tag{2.14}$$

where, in our notation, primes ($'$) applied to dimensionless functions denote differentiation with respect to the *dimensionless* coordinate S : in the expression above, $\theta' = d\theta/dS$.

The shell strains take exactly the same form as earlier in (2.10) and (2.12) when expressed in terms of the dimensionless variables,

$$\begin{aligned}E_{SS}(S, T) &= \varepsilon + \varepsilon_p(T) + v_{,S}(S, T) + \frac{1}{2}(-T\tau(S) + w_{,S}(S, T))^2 \\ &\dots \\ B_{SS}(S, T) &= -\tau'(S) T + w_{,SS}(S, T) \\ &\dots\end{aligned}\tag{2.15}$$

In (2.15), we have introduced the dimensionless pre-strain ε_p profile, see Equation (5), as

$$\varepsilon_p(T) = \begin{cases} p & \text{if } |T| \leq \frac{r}{2} \\ 0 & \text{if } \frac{r}{2} \leq |T| \leq \frac{1}{2}. \end{cases}\tag{2.16}$$

We assume that the non-scaled strain $\bar{\varepsilon}$ and pre-strain \bar{p} remain small in the experiments, implying that we can use a linearly elastic constitutive law in the shell model. By our scaling conventions in (2.13), we rescale them using a typical strain $(a k)^2 \sim (t/a)^2 \ll 1$ which is *small*: as a result, the rescaled strains ε and p are not necessarily small, see the numerical values used in Section 5.

2.2.3. Shell energy

We consider ribbons made up of a linear elastic material and write the non-dimensional strain energy of shell Φ as

$$\Phi = \frac{1}{2} \int_0^\ell \int_{-\frac{1}{2}}^{+\frac{1}{2}} \left(\frac{1}{1-\nu^2} (\nu (E_{\alpha\alpha})^2 + (1-\nu) E_{\alpha\beta} E_{\alpha\beta}) + \nu (B_{\alpha\alpha})^2 + (1-\nu) B_{\alpha\beta} B_{\alpha\beta} \right) dS dT,\tag{2.17}$$

where we use Einstein's convention on implicit summation over repeated indices, and $\ell = \frac{L}{a} = \gamma^{-1} \gg 1$ denotes the length-to-width ratio, ν is Poisson's ratio of the material. With Y as the Young modulus and t as the thickness, non-dimensional strain energy $\Phi = \bar{\Phi} / [Y t^5 / (12 a (1-\nu^2)^2)]$ derives from the (dimensional) shell strain energy $\bar{\Phi}$ used in the classical Kirchhoff plate theory, see for instance the strain energy used in equations [2.15–2.16] of [Koi60].

2.3. Solution for the cross-sectional displacements

The cross-sectional displacements $(u(S, T), v(S, T), w(S, T))$ enter the shell energy (2.17) via the expressions (2.15) of the membrane and bending strains $E_{\alpha\beta}$ and $B_{\alpha\beta}$. As they are functions of both mid-surface coordinates S and T , we aim to eliminate them to derive the one-dimensional energy functional. Following our previous line of work on variational higher-order dimension reduction [AH16; LA20b; AL21; KAL23], we do this by optimizing the shell energy (2.17) with respect to the unknowns $(u(S, T), v(S, T), w(S, T))$ being subjected to the kinematic conditions (2.9).

This optimization problem is intractable in general but can be solved in a perturbative way, thanks to the presence of the small scale separation parameter $\gamma \ll 1$, see Equation (2.2). The higher-order dimension reduction method does precisely this, by identifying series solutions for each one of the three unknown cross-sectional displacements $(u(S, T), v(S, T), w(S, T))$ in powers of $\gamma \ll 1$. The method is exactly similar to what the authors have previously done in [KAL23; LA20b], see Section-2 of [KAL23] in particular. The optimization is carried out in symbolic form in the companion Wolfram Mathematica notebook, available from the public repository [KA24]. Up to an error of order γ^2 , the result is

$$\begin{aligned}
u(S, T) &= -\frac{1}{6}\nu T^3 \tau^2(S), \\
v(S, T) &= \frac{1}{12}\tau(S) \tau'(S) \left[T^2(1+\nu) - T^4(3-\nu) + \frac{8}{5}T^6(1-\nu) - \frac{83+155\nu}{1680} \right. \\
&\quad \left. + \tau^2(S) \left(\frac{1}{1920}T^4 - \frac{1}{600}T^6 + \frac{1}{560}T^8 - \frac{23}{6451200} \right) \right. \\
&\quad \left. + \frac{1}{15}p \left[r^3 \left(\frac{3r^2}{16}T - \frac{5}{4}T^3 - \frac{15}{8}T^4 + T^6 + \frac{1}{896}(9r^4 + 42r^2 - 16) \right) \right. \right. \\
&\quad \left. \left. + \left(T - \frac{r}{2} \right)^4 \left(T^2 + 2rT + \frac{5}{8}r^2 \right) \Theta \left(T - \frac{r}{2} \right) - \left(T + \frac{r}{2} \right)^4 \left(T^2 - 2rT + \frac{5}{8}r^2 \right) \Theta \left(T + \frac{r}{2} \right) \right] \right], \\
w(S, T) &= \tau'(S) \left[\frac{1}{560}(11-25\nu)T - \frac{1}{6}(1-2\nu)T^3 + \frac{1}{5}(1-\nu)T^5 \right. \\
&\quad \left. + \tau^2(S) \left(-\frac{41}{4838400}T + \frac{1}{11520}T^3 - \frac{1}{4800}T^5 + \frac{1}{5040}T^7 \right) \right. \\
&\quad \left. + \frac{1}{120}p \left[r^3 \left(\frac{3}{112}T(r^4 - 14r^2 - 22) - \frac{5}{2}T^2 - \frac{5}{2}T^3 + T^5 - \frac{r^2}{8} \right) \right. \right. \\
&\quad \left. \left. + \left(T - \frac{r}{2} \right)^4 (T+2r) \Theta \left(T - \frac{r}{2} \right) - \left(T + \frac{r}{2} \right)^4 (T-2r) \Theta \left(T + \frac{r}{2} \right) \right] \right],
\end{aligned} \tag{2.18}$$

where Θ is the Heaviside function defined by $\Theta(\tilde{T}) = 1$ if $\tilde{T} \geq 0$ and $\Theta(\tilde{T}) = 0$ otherwise.

In view of the fundamental assumption (2.2) of scale separation, the scaled one-dimensional twisting strain $\tau(S)$ and its derivatives are respectively of order

$$\tau(S) = \mathcal{O}(\gamma^0), \quad \tau'(S) = \mathcal{O}(\gamma^1), \quad \tau''(S) = \mathcal{O}(\gamma^2), \quad \dots \tag{2.19}$$

These scaling assumptions are implicit in our notation: each differentiation, denoted by a prime, counts as γ as far as scaling analysis is concerned. The solution $u(S, T)$ in (2.18)₁ therefore starts at order γ^0 and has a vanishing term of order γ^1 , while the solutions $v(S, T)$ and $w(S, T)$ in (2.18)_{2,3} start at order γ^1 .

2.4. Second-order approximation of the strain

Next, we insert the solution (2.18) for the cross-sectional displacement into the expressions (2.15) of the membrane and bending strains $E_{\alpha\beta}$ and $B_{\alpha\beta}$. This yields new expressions for the strain, in the form

$$\begin{aligned}
e_{SS}(S, T) &= \frac{\mathcal{O}(\gamma^0)}{\varepsilon + \varepsilon_p(T) + \frac{1}{2}T^2 \tau^2(S)} & \frac{\mathcal{O}(\gamma^1)}{+v_{,S} - \frac{1}{2}T\tau(S)w_{,S}} & \frac{\mathcal{O}(\gamma^2)}{+ \frac{1}{2}w_{,T}^2} \\
e_{TT}(S, T) &= -\nu(\varepsilon + \varepsilon_p(T)) + u_{,T} & & \\
e_{ST}(S, T) &= \frac{1}{2}(\tau(S)(w - Tw_{,T}) + v_{,T} + u_{,S}) & & \\
b_{SS}(S, T) &= -T\tau'(S) & & \\
b_{TT}(S, T) &= w_{,TT} & & \\
b_{ST}(S, T) &= -\tau(S) & & + w_{,ST}.
\end{aligned} \tag{2.20}$$

The strain $e_{\alpha\beta}$ and $b_{\alpha\beta}$ in equation above have been obtained by inserting the order- γ solution for the displacement in (2.18) into the original strain $E_{\alpha\beta}$ and $B_{\alpha\beta}$ in (2.15) and by *truncating the result beyond order γ^2* . In Equation (2.20), the contributions have been sorted in columns by decreasing order of magnitude. In the interest of

legibility, we have omitted the arguments S, T of the functions $u(S, T)$, $v(S, T)$ and $w(S, T)$ in the right-hand sides.

It is remarkable that the error of order γ^2 in the displacements (2.18) allows the strain in (2.20) to be resolved with a smaller error, of order γ^3 . Take the $v_{,S}$ term appearing in e_{SS} , for instance: v is given by (2.18) as a quantity proportional to τ' (hence of order γ) plus an error term of order γ^2 . Differentiating one more time with respect to the slow variable S entails multiplying by $\gamma \ll 1$, so that $v_{,S}$ is proportional to τ'' and τ'^2 (hence of order γ^2 , as indicated by the column heading) plus an *error term of order γ^3* . A similar argument holds for all the contributions to $e_{\alpha\beta}$ and $b_{\alpha\beta}$, and we conclude that the truncation error in (2.20) is

$$\begin{aligned} E_{\alpha\beta} &= e_{\alpha\beta} + \mathcal{O}(\gamma^3), \\ B_{\alpha\beta} &= b_{\alpha\beta} + \mathcal{O}(\gamma^3). \end{aligned} \quad (2.21)$$

2.5. Ensuring positiveness of the energy

Next, we calculate the strain energy density defined in (2.17) based on the *truncated* version of the strains $e_{\alpha\beta}$ and $b_{\alpha\beta}$ obtained in (2.20). Denoting the result as Φ^* , we have

$$\Phi^* = \frac{1}{2} \int_0^\ell \int_{-\frac{1}{2}}^{+\frac{1}{2}} \left(\frac{1}{1-\nu^2} (\nu (e_{\alpha\alpha})^2 + (1-\nu) e_{\alpha\beta} e_{\alpha\beta}) + (\nu (b_{\alpha\alpha})^2 + (1-\nu) b_{\alpha\beta} b_{\alpha\beta}) \right) dS dT. \quad (2.22)$$

In view of (2.21), this approximation Φ^* of the shell energy Φ is exact up to an error of order γ^3 ,

$$\Phi = \Phi^* + \mathcal{O}(\gamma^3). \quad (2.23)$$

The energy being quadratic in the strain $e_{\alpha\beta}$ and $b_{\alpha\beta}$, it contains not only terms of order γ^0 , γ^1 and γ^2 but also terms of order γ^3 and γ^4 , such as for instance a $v_{,S}^2 = \mathcal{O}(\gamma^4)$ term coming from the expansion of the $v_{,S}$ term in the trace square term $(e_{\alpha\alpha})^2 = (e_{SS} + \dots)^2 = (\dots + v_{,S} + \dots)^2$. In all our previous work on dimensional reduction [AH16; LA20b; AL21; KAL23], we truncated the energy Φ^* beyond order γ^2 , the motivation being that terms of order γ^3 are comparable to the approximation error in (2.23). *Here, by contrast, we refrain from truncating the energy Φ^* in (2.22), and retain the negligible terms of order γ^3 and γ^4 .* As we will show, this is a critically important point ensuring that the one-dimensional model is useable in numerical simulations. Truncating the energy Φ^* as we did in previous work raises severe mathematical difficulties that had escaped to us so far.

For the moment, it will suffice to note that the strain energy density Φ^* in (2.22) is positive,

$$\Phi^* \geq 0, \quad (2.24)$$

as its integrand is a sum of squares. This positiveness property would break if we were to truncate Φ^* , by dropping terms at order γ^3 and beyond.

These higher-order terms are *not* asymptotically correct: to determine their actual value, one would need to push the dimension reduction procedure to higher-order. That does not mean they are useless, however.

2.6. One-dimensional energy obtained by integrating along the width

On inserting the displacements in (2.18) and strains in (2.20), we can obtain an explicit expression for the strain energy density appearing in the integrand of (2.22). Integrating it along the width, we obtain the one-dimensional energy $\Phi^*[\tau]$ in the form announced earlier in (2.1),

$$\Phi^*[\tau] = \int_0^\ell W(p, r, \varepsilon; \tau(S), \tau'(S), \tau''(S)) dS + [W_b(p, r; \tau(S), \tau'(S))]_0^\ell, \quad (2.25)$$

where W is the one-dimensional strain energy density and W_b is the strain energy contribution from boundaries at ribbon ends $S=0$ and $S=\ell$. The explicit forms for W and W_b are given below.

The boundary term $[W_b]_0^\ell$ are produced by an additional integration by parts with respect to the arc-length S , as we briefly explain now. Integrating (2.22) along the width first yields a one-dimensional strain energy density that includes a term of the form

$$\int_0^\ell \left(\dots + C(p, r; \tau(S)) \tau(S) \tau''(S) + 3H(p, r; \tau(S)) \tau(S) \tau'^2(S) \tau''(S) + \dots \right) dS. \quad (2.26)$$

To remove the τ'' terms, we integrate this term by part with respect to the S -coordinate. This produces a boundary term of the form $[C(p, r; \tau) \tau \tau' + H(p, r; \tau) \tau \tau'^3]_0^\ell$ which is nothing but W_b , see (2.30). The detailed calculations can be found in the companion notebook [KA24].

The one-dimensional strain energy density W is obtained in the form

$$W(p, r, \varepsilon; \tau, \tau', \tau'') = \frac{1}{2} \left(\underbrace{A(p, r, \varepsilon; \tau)}_{\gamma^0} + \underbrace{B(p, r; \tau) \tau'^2}_{\gamma^2} + \underbrace{F(p, r; \tau) \tau''^2 + G(p, r; \tau) \tau'^4}_{\gamma^4} \right) \quad (2.27)$$

where the horizontal braces are used to group the contributions by order of magnitude, see (2.19). The energy density A at order γ^0 and the coefficients B , F and G associated with the gradient effect are all polynomials in τ containing only even powers of τ ,

$$\begin{aligned} A(p, r, \varepsilon; \tau) &= A_0 + A_2 \tau^2 + A_4 \tau^4 & F(p, r; \tau) &= F_0 + F_2 \tau^2 + F_4 \tau^4 + F_6 \tau^6 \\ B(p, r; \tau) &= B_0 + B_2 \tau^2 + B_4 \tau^4 & G(p, r; \tau) &= G_0 + G_2 \tau^2 + G_4 \tau^4 + G_6 \tau^6 + G_8 \tau^8. \end{aligned} \quad (2.28)$$

The coefficients A_i , B_i , F_i and G_i are known functions of the pre-strain p , Poisson's ratio ν and of the aspect-ratio r —the quantities A_0 and A_2 have an additional dependence on the applied strain ε . The expressions of the following set of coefficients are crucial for the rest of the analysis:

$$\begin{aligned} A_0(p, r, \varepsilon) &= \varepsilon^2 + pr(2\varepsilon + p) \\ A_2(p, r, \varepsilon) &= \frac{1}{12} (24(1-\nu) + \varepsilon + pr^3) \\ A_4(p, r) &= \frac{1}{320} \\ B_0(p, r) &= \frac{1}{420} \left[-71\nu^2 + 44\nu + 27 + \frac{1}{8} pr^3(1-r^2)(-25\nu - 3(1-\nu)r^2 + 11) \right. \\ &\quad \left. + \frac{1}{64} p^2 r^6 (1-r^2)^2 (r^2 + 2r - 11) \right] \\ F_0(p, r) &= \frac{1-\nu}{441 \cdot 10^2} \left[365\nu^2 - 268\nu + 50 \right. \\ &\quad \left. + \frac{pr^3}{96} (1-r^2)(2267\nu - 35(1-\nu)r^4 + (316 - 694\nu)r^2 - 881) \right. \\ &\quad \left. + \frac{p^2 r^6}{18432} (81r^8 - 476r^6 - 12258r^4 + 44800r^3 - 41580r^2 + 9433) \right]. \end{aligned} \quad (2.29)$$

The other coefficients $F_2, \dots, F_6, G_0, \dots, G_8$ are given in Appendix B and can also be found in the companion notebook [KA24]. This completes the definition of the integral term W in (2.25).

The boundary term in (2.25) has been obtained in the form

$$\begin{aligned} [W_b(p, r; \tau, \tau')]_0^\ell &= \int_0^\ell \left(\underbrace{(C(p, r; \tau) \tau \tau')}'_{\gamma^2} + \underbrace{(H(p, r; \tau) \tau \tau'^3)}'_{\gamma^4} \right) dS \\ &= \left[C(p, r; \tau) \tau \tau' + H(p, r; \tau) \tau \tau'^3 \right]_0^\ell, \end{aligned} \quad (2.30)$$

where

$$\begin{aligned} C(p, r; \tau) &= C_0 + C_2 \tau^2 + C_4 \tau^4 \\ H(p, r; \tau) &= H_0 + H_2 \tau^2 + H_4 \tau^4 + H_6 \tau^6. \end{aligned} \quad (2.31)$$

The expressions of the coefficients $C_i = C_i(p, r, \nu)$ and $H_i = H_i(p, r, \nu)$ can be found in Appendix B and in the companion notebook [KA24].

3. MAIN FEATURES OF THE ONE-DIMENSIONAL MODEL

This section discusses the qualitative features of the one-dimensional energy derived in (2.27). The energy is composed of terms of order γ^0 , γ^2 and γ^4 : the leading-order terms, the second-order terms capturing the gradient effect, and the fourth-order terms are discussed in Sections 3.1, 3.2 and 3.3, respectively. Further, Section 3.4 presents the variational derivation of the equilibrium boundary-value problem.

3.1. Leading-order energy is non-convex

The strain energy density at order γ^0 has been obtained in recent work [GRA23]. It is given by (2.27) and (2.29)₁ as

$$\begin{aligned} \Phi^*|_{\gamma^0} &= \int_0^\ell \frac{1}{2} A(p, r, \varepsilon; \tau(S)) dS \\ &= \int_0^\ell \frac{1}{2} (A_0(p, r, \varepsilon) + A_2(p, r, \varepsilon) \tau^2(S) + A_4(p, r) \tau^4(S)) dS. \end{aligned} \quad (3.1)$$

In the remainder of this section, we briefly recall the main mathematical features of the function $A(p, r, \varepsilon; \tau)$ reported in [GRA23] and their connection with twist buckling.

A necessary condition for $\Phi^*|_{\gamma^0}$ to be a convex functional of τ is that its second derivative is positive at the particular point $\tau=0$:

$$\begin{aligned} \left. \frac{\partial^2 A(p, r, \varepsilon; \tau)}{\partial \tau^2} \right|_{\tau=0} &= A_2(p, r, \varepsilon) \\ &= 2(1-\nu) + \frac{\varepsilon + r^3 p}{12}. \end{aligned} \quad (3.2)$$

When the imposed average strain ε is compressive enough, $\varepsilon < -(r^3 p + 24(1-\nu))$, the necessary condition $\partial^2 A / \partial \tau^2 \geq 0$ is not satisfied, implying that $\Phi^*|_{\gamma^0}$ is *not convex* with respect to τ . At the critical point when $\varepsilon = 0$, the planar configuration $\tau \equiv 0$ becomes unstable with respect to twist perturbations and twist buckling takes place.

The right-hand side of (3.2) is the *tangent twist modulus*, and has three contributions:

- The term $2(1-\nu)$ is the non-dimensional twist stiffness for a thin ribbon, akin to the twist stiffness of a Kirchhoff rod. It is always positive, hence stabilizing with respect to twist perturbations.
- The term $\varepsilon/12$ captures the coupling between longitudinal applied strain and twisting. It is destabilizing when ε is more and more compressive (*i.e.*, negative).
- The term $r^3 p/12$ captures the effect of *inhomogeneous* pre-stress across the width. This term is positive (since $p > 0$ in the central region) and enhances the stability of the ribbon. A key feature of this term is that for large enough values of the pre-strain p , the twist instability may take place *before* Euler buckling as the ribbon's end-to-end distance decreases (that is, when ε decreases): although the $r^3 p/12$ term stabilizes the ribbon for fixed end-to-end distance (*i.e.*, fixed ε), it is instrumental for the twist instability to win over the Euler instability in at least some range of values of ε .

The competition between twist and Euler buckling is discussed in detail [GRA23]. With $N = \frac{\partial W}{\partial \varepsilon}(p, r, \varepsilon; \tau \equiv 0) = \varepsilon + rp$ as the internal longitudinal force in the ribbon, the critical load for Euler buckling is given in an infinitely long ribbon by the condition $N = 0$, thus giving the critical strain for Euler buckling as

$$\varepsilon_{\text{Euler}}^* = -rp. \quad (3.3)$$

In the present work, we limit attention to twisted configurations arising *before* Euler buckling sets in, for $\varepsilon > \varepsilon_{\text{Euler}}^*$.

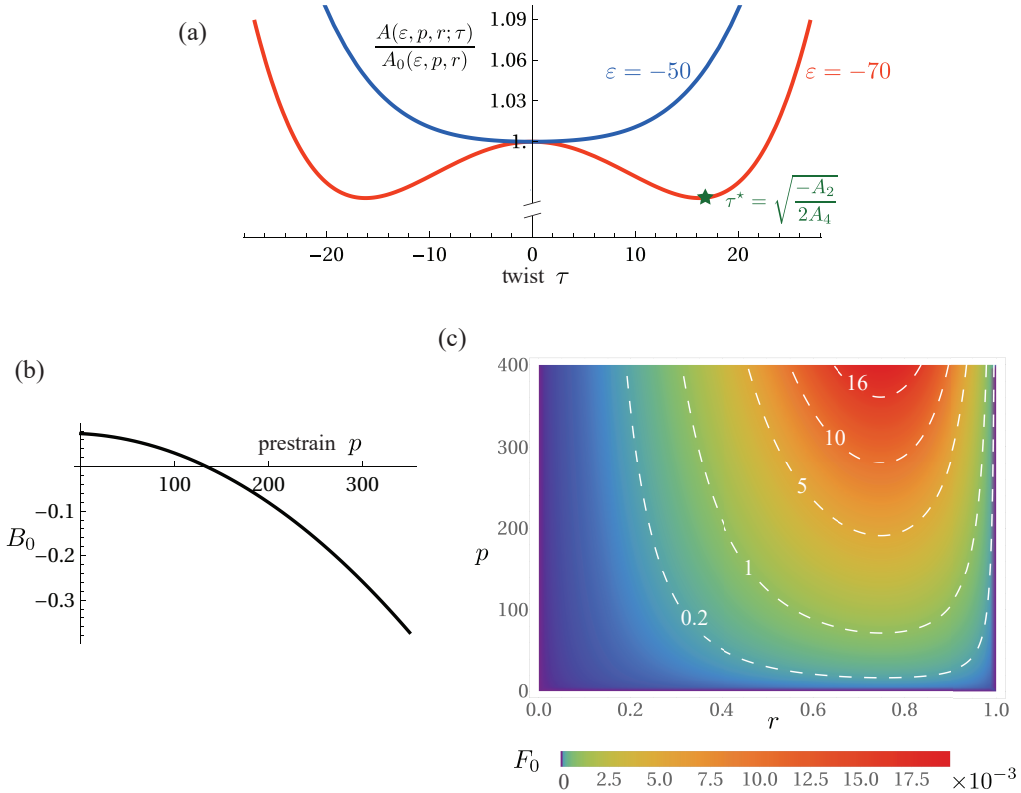


Figure 3.1. Plots of important energy terms appearing in (2.27–2.29), for Poisson's ratio $\nu = 1/2$. (a) Scaled energy per unit length $A(p, r, \varepsilon; \tau)/2$ at leading order versus τ for width ratio $r = 2/3$ and scaled pre-strain $p = -145.58$: the profile is convex for moderate end-to-end shortening (scaled axial strain $\varepsilon = -50$, blue curve) and becomes non-convex for more severe end-to-end shortening ($\varepsilon = -70$, red curve); the loss of convexity (onset of twist buckling) takes place at $\varepsilon = -55.1348$. (b) Incremental gradient modulus $B_0 = B(p, r = 2/3; \tau = 0)$ evaluated in the planar configuration ($\tau = 0$) as a function of pre-strain p . Later in this paper, we will connect the change of sign in B_0 to the transition from long- to short-wavelength buckling. (c) Fourth-order term $F_0(p, r) > 0$ is always positive. This warrants that the overall energy remains positive against very short-wavelength perturbations ($q \rightarrow \infty$), even when the second-order gradient modulus B_0 is negative.

As shown in Figure 3.1(a), for given values of ε , p and r , the quadratic potential in (3.1) has a single minimum $\tau = 0$ in the convex case $A_2(p, r, \varepsilon) \geq 0$. In the non-convex case, $A_2(p, r, \varepsilon) < 0$, a bifurcation takes place and the central equilibrium $\tau = 0$ becomes a local maximum (unstable equilibrium) with two symmetric minima $\tau = \pm\tau^*(\varepsilon)$ (stable equilibria), where

$$\tau^*(\varepsilon) = \sqrt{\frac{-A_2(p, r, \varepsilon)}{2A_4(p, r)}}. \quad (3.4)$$

By Equation (2.29)₃, the coefficient A_4 (and, thus, the argument of the square root) is always positive.

The analysis of twist buckling proposed in [GRA23] is based on the leading-order energy $\Phi^*|_{\gamma^0}$ and bears the same limitations as highlighted in the classical analysis of a non-convex elastic bars by Ericksen [Eri75]. It accounts for a bifurcation on the *unsigned* value τ^* of the order parameter, see (3.4), but cannot predict (i) how the *sign* of $\tau(S)$ is distributed in space (local handedness of the helical buckling pattern), nor (ii) the existence of smooth transition regions, known as *perversions* [DH05], that connect ‘phases’ having opposite signs of τ . In the leading-order model, these perversions are rendered as points of discontinuity where $\tau(S)$ flips sign (see §3.7 in [GRA23]), and there is no control on the number of such discontinuities nor on their distribution in space.

3.2. Gradient effect is captured by second-order terms

Our main contribution is to account for this gradient effect by including the higher-order terms in the one-dimensional model (2.27), in line with previous work analyzing localized deformations in slender structures such as the necking of elastic bars [AH16] or elasto-capillary cylinders [LA20a] and propagating bulges in cylindrical balloons [LA18; YF23]. The gradient effect appears at order γ^2 in the one-dimensional energy, see (2.27) and (2.30),

$$\Phi^*|_{\gamma^2} = \int_0^\ell \frac{1}{2} B(p, r; \tau) \tau'^2 dS + [C(p, r; \tau) \tau \tau']_0^\ell \quad (3.5)$$

Taking this regularization into account will enable us to resolve the inner structure of perversions and to predict their distribution along the ribbon length, see Section 5. The gradient effect in $\Phi^*|_{\gamma^2}$ has been derived in Section 2. Even though the dimension reduction procedure which we have used warrants asymptotic correctness in principle, we have introduced two simplifying approximations along the way that break asymptotic correctness at order γ^2 :

- we have neglected the longitudinal variations of the axial strain $\bar{\varepsilon}(\bar{S})$ in Section 2.2,
- the cross-sectional displacements produced by dimension reduction satisfy the clamping conditions $(u, v, w) = 0$ in an average sense only, but not for all values of the transverse coordinate T . This incompatibility between the boundary conditions applicable to the shell model which we started from, and those which the dimension reduction procedure can ultimately handle point to the presence of boundary layers forming near the clamps. Accounting for boundary layers through effective boundary conditions is an active topic of research, both in the context of higher-order dimension reduction and homogenization [TAL24], and we will ignore this difficulty.

We assume that these approximations do not significantly affect the analysis of twist buckling. The influence of boundary layers, in particular, can be expected to be limited to vicinity of the clamps.

In the unbuckled configuration, the gradient modulus (*i.e.*, the coefficient in factor or $\tau'^2/2$ in the energy) is given by $B(p, r; \tau = 0) = B_0$. This quantity is plotted in Figure 3.1(b) and appears to change sign depending on the amount of pre-strain p . Negative gradient moduli $B_0 < 0$ are commonly encountered in higher-order dimension reduction, including in the linear setting—see the illustration examples in [LA20b; KAL23] for instance: they are considered inconsistent as they make *any* equilibrium solution unstable with respect to infinitesimal, short-wavelength oscillations. In Appendix A, we indeed calculate the energy $\Phi^*|_{\gamma^0} + \Phi^*|_{\gamma^2}$, truncated at order γ^2 , of a solution having a harmonic twist angle distribution $\theta(S) = \sin(qS)/q$ and show that $(\Phi^*|_{\gamma^0} + \Phi^*|_{\gamma^2}) \rightarrow -\infty$ when the modulation becomes very short-wavelength ($q \rightarrow \infty$), whenever $B_0 < 0$. This is contradictory, since the strain energy cannot be less than its value (0) in the relaxed configuration shown in Figure 2.1(a).

We show that this is a truncation issue and fix it by including non-asymptotic terms of order γ^4 in the energy, as discussed in Section 3.3 below.

We will also show that the sign of B_0 governs the competition between short- and long-wavelength buckling, see Section 4. To the best of our knowledge, this is the first time that negative values of the tangent gradient modulus B_0 are connected to a real phenomenon and not just viewed as an undesirable outcome of higher-order dimension reduction or homogenization.

3.3. Non-asymptotic fourth-order terms ensure positiveness

The fourth-order terms in the energy (2.27) take the form

$$\Phi^*|_{\gamma^4} = \int_0^\ell \frac{1}{2} (F(p, r; \tau) \tau''^2 + G(p, r; \tau) \tau'^4) dS + [H(p, r; \tau) \tau \tau'^3]_0^\ell \quad (3.6)$$

They are not asymptotically exact, as noted at the end of Section 2.5. They ensure positiveness of the energy, see (2.24). In particular, it is shown in Figure 3.1(c) that the coefficient $F_0 = F(p, r; \tau = 0)$ is positive for the range of parameter values considered in this paper, $r \in [0, 1]$, $\nu \in [0, 1/2]$ and $\bar{p} \in [0, 1]$. The minimum value of F_0 is calculated in the Supplementary material [KA24] and it is found positive.

The positiveness brought about by the $\Phi^*|_{\gamma^4}$ terms is instrumental in making the one-dimensional model usable in numerical simulations. It comes with a price, however, which is to increase the maximum order of differentiation in the energy, from 1 (τ' term present in the expression $\Phi^*|_{\gamma^2}$) to 2 (τ'' term in the expression of $\Phi^*|_{\gamma^4}$). In terms of the primary kinematic variable θ , the order of differentiation is 3 ($\tau'' = \theta'''$), implying that the equilibrium problem will be of order 6, and not just 4 as for the truncated (but dysfunctional) energy $\Phi^*|_{\gamma^0} + \Phi^*|_{\gamma^2}$.

3.4. Variational derivation of equilibrium equations

In the next sections, we predict equilibrium configurations of the ribbon based on the one-dimensional model for same *clamped* boundary conditions as in the experiments [GRA23],

$$\theta(0) = 0, \quad \theta(\ell) = 0. \quad (3.7)$$

The longitudinal displacement imposed by the clamps is taken into account via the mean axial strain ε , see (2.6).

The equilibrium equations for the ribbon are now derived by deriving the Euler–Lagrange stationarity condition of the one-dimensional energy Φ^* in (2.25). For any configuration $\theta(S)$ satisfying the kinematical boundary conditions (3.7), we consider a kinematically admissible perturbation $\delta\theta(S)$, such that $\delta\theta(0) = \delta\theta(\ell) = 0$. The first variation of the strain energy Φ^* in (2.25) takes the form

$$\delta\Phi^* = \int_0^\ell \left(\frac{\partial W}{\partial \tau} \delta\tau + \frac{\partial W}{\partial \tau'} \delta\tau' + \frac{\partial W}{\partial \tau''} \delta\tau'' \right) dS + \left[\frac{\partial W_b}{\partial \tau} \delta\tau + \frac{\partial W_b}{\partial \tau'} \delta\tau' \right]_0^\ell, \quad (3.8)$$

where $\delta\tau = \delta\theta'$ denotes the increment of twisting strain, see (2.14). After two integrations by parts, we get

$$\delta\Phi^* = \int_0^\ell \left(\frac{\partial W}{\partial \tau} - \frac{d}{dS} \left(\frac{\partial W}{\partial \tau'} \right) + \frac{d^2}{dS^2} \left(\frac{\partial W}{\partial \tau''} \right) \right) \delta\tau dS + \left[\left(\frac{\partial W_b}{\partial \tau} + \frac{\partial W}{\partial \tau'} - \frac{d}{dS} \left(\frac{\partial W}{\partial \tau''} \right) \right) \delta\tau + \left(\frac{\partial W_b}{\partial \tau'} + \frac{\partial W}{\partial \tau''} \right) \delta\tau' \right]_0^\ell. \quad (3.9)$$

We identify the internal twisting moment $M(S)$ as the quantity in factor of $\delta\tau(S)$ in the integral term,

$$M = \frac{\partial W}{\partial \tau} - \frac{d}{dS} \frac{\partial W}{\partial \tau'} + \frac{d^2}{dS^2} \frac{\partial W}{\partial \tau''}. \quad (3.10)$$

Using $\delta\tau = \delta\theta'$ and integrating by parts one more time, one can rewrite $\delta\Phi^*$ as

$$\delta\Phi^* = - \int_0^\ell \frac{dM}{dS} \delta\theta dS + \left[M \delta\theta + \left(\frac{\partial W_b}{\partial \tau} + \frac{\partial W}{\partial \tau'} - \frac{d}{dS} \left(\frac{\partial W}{\partial \tau''} \right) \right) \delta\tau + \left(\frac{\partial W_b}{\partial \tau'} + \frac{\partial W}{\partial \tau''} \right) \delta\tau' \right]_0^\ell. \quad (3.11)$$

This first variation has to be zero for any perturbation $\delta\theta$ satisfying $\delta\theta(0) = \delta\theta(\ell) = 0$. This leads to the balance of twisting moments in the interior

$$\frac{dM}{dS} = 0, \quad (3.12)$$

and the two boundary conditions, applicable at both $S=0$ and $S=\ell$,

$$\begin{cases} \left[\frac{\partial W_b}{\partial \tau} + \frac{\partial W}{\partial \tau'} - \frac{d}{dS} \left(\frac{\partial W}{\partial \tau''} \right) \right]_{S=0,\ell} = 0, \\ \left[\frac{\partial W_b}{\partial \tau'} + \frac{\partial W}{\partial \tau''} \right]_{S=0,\ell} = 0. \end{cases} \quad (3.13)$$

Along with the kinematic boundary conditions (3.7), the differential equation (3.12), the constitutive law (3.10) and the static boundary conditions (3.13) make up a well-posed boundary-value problem: the differential equation for $\theta(S)$ is of order 6, and there are 3 boundary conditions at each end. The balance of twisting moments in (3.12) takes the same form as in the twisting of classical bars. The constitutive relation (3.10), however, corrects the constitutive relation $M = \partial W / \partial \tau$ applicable to classical bars with higher-order corrections. The boundary conditions (3.13) are not present in the twisting of classical bars, and arise because the order of the equilibrium equation has increased from 2 (classical bars) to 6 here. As discussed in Section 3.3, the order 6 breaks down into $2+2+2$, where the first 2 is the order of the classical bar model, the second 2 comes from the fact that we include the gradient effect, and the final 2 is an additional fee for retaining the terms of order γ^4 ensuring positiveness. As discussed in Section 3.2, the boundary conditions (3.13) are not asymptotically exact as we ignore the boundary layers forming near the clamp. Yet, the boundary-value problem is derived *variationally*, which makes it mathematically consistent.

The boundary-value problem derived above is used in Section 4 to set up a linear bifurcation analysis addressing the wavelength selection, and in Section 5 to analyze the post-buckled solutions numerically.

4. ONSET OF BUCKLING IN AN INFINITELY LONG RIBBON

This section addresses the competition of short- and long-wavelength buckling sketched in Figure 1.1, based on the one-dimensional model. We focus on the case of an infinitely long ribbon and therefore ignore the boundary conditions (3.7) and (3.13). In Sections 4.1-4.3, we carry out a linear bifurcation analysis: we identify the bifurcation points at which new solution branches emerge from the planar configuration $\tau \equiv 0$, and compute the associated critical end-to-end distance ε and critical wavenumber q . In this infinite-length setting, we postulate that the long-wavelength case corresponds to a vanishing first critical wavenumber $q = 0$, and the short-wavelength case to a non-vanishing first critical wavenumber $q > 0$. This postulate will be confirmed in Section 5 by numerical simulations of finite-length ribbons. In Section 4.4, we derive a weakly non-linear solution describing a perversion connecting two two infinitely long helical phases with opposite chiralities.

4.1. Linearized equilibrium about a planar configuration

For given applied strain ε , we consider the planar configuration of ribbon shown in Figure 2.1(c), whose twisting strain is identically zero, $\tau \equiv 0$. We denote as $\tau(S)$ the perturbation to the twist about the planar state and derive an expansion of the strain energy density to order $|\tau|^2$. In view of (2.25–2.27), the quadratic terms in the expansion are given by

$$W = \frac{1}{2} (A_0 + A_2 \tau^2 + B_0 \tau'^2 + F_0 \tau''^2). \quad (4.1)$$

The constitutive relation (3.10) then yields a linear approximation of the internal moment M as

$$M = A_2 \tau - B_0 \tau'' + F_0 \tau^{(4)}, \quad (4.2)$$

and the equilibrium (3.12) is linearized as

$$F_0 \frac{d^5 \tau}{dS^5} - B_0 \frac{d^3 \tau}{dS^3} + A_2 \frac{d\tau}{dS} = 0. \quad (4.3)$$

4.2. Long- versus short-wavelength instabilities

The bifurcation equation (4.3) has constant coefficients and we can limit attention to modes that depend harmonically on the arc-length coordinate S : using complex notations, we set the mode as $\theta(S) = \theta_0 e^{iqS}$, hence $\tau(S) = \theta'(S) = iq \theta_0 e^{iqS}$, where q is the wavenumber and θ_0 the amplitude of the mode. Inserting into (4.3), we get

$$q^2 \theta_0 (F_0(p, r) q^4 + B_0(p, r) q^2 + A_2(p, r, \varepsilon)) = 0. \quad (4.4)$$

The factor q^2 yields a double root $q = 0$ which corresponds to (i) a uniform rigid-body rotation about the axis (constant $\theta(S)$), and (ii) a uniform twist (helical) mode (linear $\theta(S)$, constant $\tau(S)$). Both these modes are prevented by the clamps at long ribbon ends, so we discard the overall q^2 factor in (4.4). We also discard the θ_0 factor, whose vanishing yields to modes that are identically zero.

Observing that the only dependence of the remaining factor on the imposed strain ε takes place through the A_2 term, we insert the expression (2.29) of A_2 into the linear bifurcation condition (4.4) and get

$$\varepsilon(q) = -(pr^3 + 12(2(1-\nu) + B_0(p, r)q^2 + F_0(p, r)q^4)). \quad (4.5)$$

This dispersion relation connects the critical stretch $\varepsilon(q)$ and the wavenumber q . It is plotted in the form of a parametric curve in the plane $(q, -\varepsilon(q))$ in Figure 4.1(a,b). In the experiments, the imposed strain ε is progressively *decreased*, *i.e.*, the quantity $(-\varepsilon)$ increases. The instability that appears first thus corresponds to the minimum of $-\varepsilon(q)$ with respect to q , *i.e.*, to the left-most point on the dispersion curve shown by a green star in the figures.

The sign of the incremental gradient modulus B_0 sets the concavity of the curve at the intersection $q = 0$ with the horizontal axis, and two scenarios are possible depending on the sign of B_0 :

- When the incremental gradient modulus is positive, $B_0 > 0$, as illustrated in Figure 4.1(a), the left-most point on the bifurcation curve (red curve) is the ‘tip’, having $q^* = 0$ (green star). The planar configuration is then expected to be stable for $-\varepsilon < -\varepsilon^*$ and becomes unstable with respect to a long-wavelength mode at $-\varepsilon = -\varepsilon^*$. Indeed, we postulate that the critical wavelength $q^* = 0$ found in this infinite-length setting will give rise to a critical wavelength comparable to the ribbon *length* in a finite-length setting. This will be confirmed numerically in Section 5.
- When the incremental gradient modulus is negative, $B_0 < 0$, as illustrated in Figure 4.1(b), the left-most point on the bifurcation curve (red curve) lies on the ‘hump’ overhanging the horizontal axis and having $q^* > 0$ (green star). The planar configuration is then expected to be stable for $-\varepsilon < -\varepsilon^*$ and to become unstable with respect to a *short-wavelength* mode at $-\varepsilon = -\varepsilon^*$. In our scaled units, $q^* = \mathcal{O}(1)$, corresponds to wavenumber $\bar{q}^* = \mathcal{O}(1/a)$, *i.e.*, to a wavelength comparable to the *width* of the ribbon. In this short-wavelength case, the critical strain ε^* (green star) differs from the critical strain $\varepsilon(0)$ associated with slowly-varying perturbations.

The wavelength selection discussed above is based on the *one-dimensional* model. It is mathematically similar to the wavelength selection proposed in [LA17] based on a *two-dimensional* plate model and a *three-dimensional* rectangular block. The one-dimensional model delivers a simpler picture which highlights the key role played by the incremental gradient modulus B_0 .

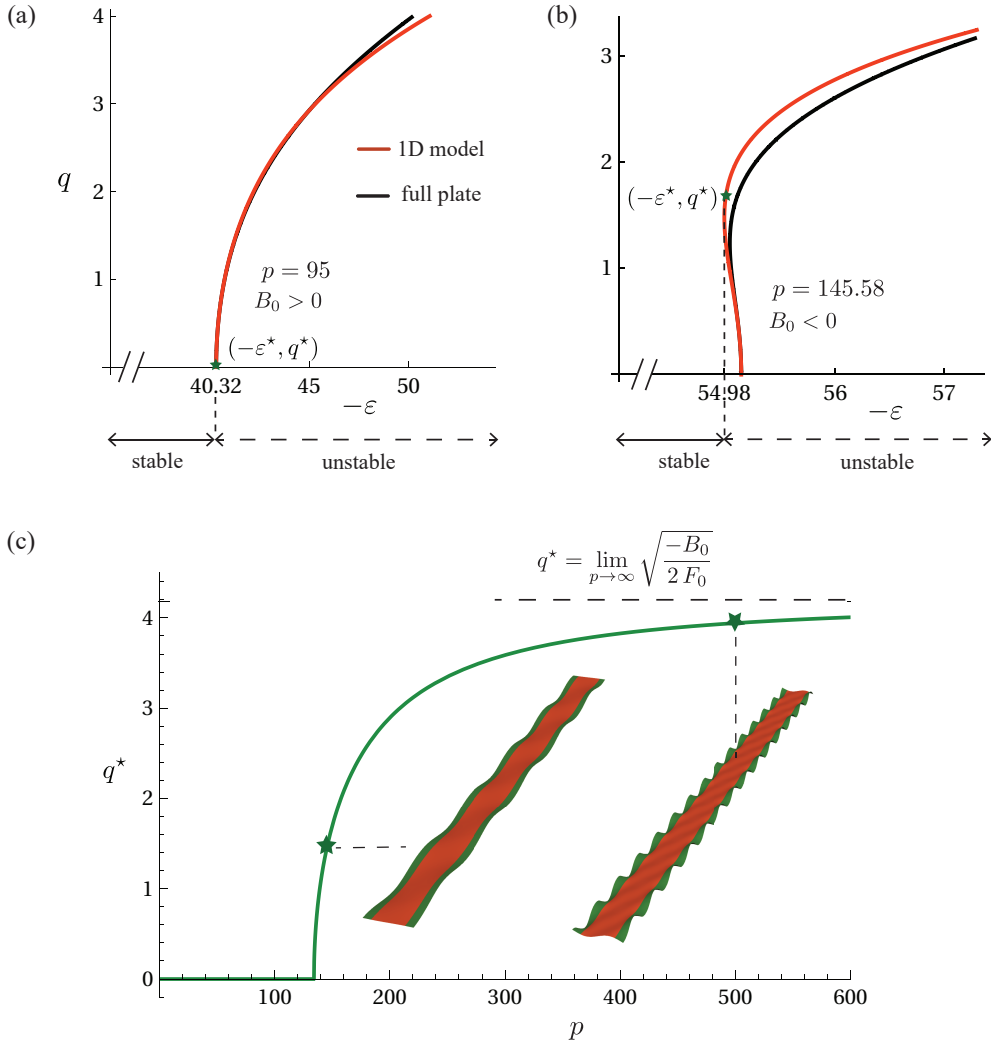


Figure 4.1. Wavelength selection in the linear bifurcation analysis of an infinitely long ribbon using the one-dimensional model (2.25), for a width ratio $r=2/3$ and Poisson's ratio $\nu=0.5$. (a) Curve of marginal stability predicted by Equation (4.5) in a case of *moderate pre-strain*, $p=95$: the incremental gradient modulus is positive, $B_0>0$, and the first unstable mode is *long-wavelength* ($q^*=0$, green star). (b) Case of *larger pre-strain*, $p=145.58$: the incremental gradient modulus is negative, $B_0<0$, and the first unstable mode is *short-wavelength* ($q^*=\mathcal{O}(1)$, green star). The predictions of a plate model adapted from Section 4 in [LA17] are included (black curves) and agree closely with the predictions of the one-dimensional model, especially in the limit $q\rightarrow 0$ of slowly varying twist. (c) Wavenumber at instability as a function of pre-strain p , as given by (4.6): the critical modes at particular values $p=145.58$ and $p=500$ are plotted using an arbitrary amplitude; the plot for $p=145.58$ correspond to the mode identified in part (b) of this figure. There is a rigid-body rotation mode corresponding to $p=95$ in part (a), which is not shown in the figure.

We proceed to derive the first critical wavenumber q^* and applied axial strain ε^* by solving the extremality condition $\varepsilon'(q^*)=0$. Using the expression of $\varepsilon(q)$ in (4.5) and recalling $F_0>0$, see Figure 3.1c, we get

$$q^* = \begin{cases} 0 & \text{if } B_0>0 \text{ (long-wavelength)} \\ \sqrt{\frac{-B_0}{2F_0}} & \text{if } B_0<0 \text{ (short-wavelength)} \end{cases} \quad (4.6)$$

$$\varepsilon^* = -(pr^3 + 24(1-\nu)) + \begin{cases} 0 & \text{if } B_0>0 \\ \frac{3B_0^2}{F_0} & \text{if } B_0<0. \end{cases}$$

These expressions have been used to position the green stars in Figure 4.1(a,b) and to generate the green curve in Figure 4.1(c).

Figure 4.1(c) echoes experimental results from prior work, see for instance Figure 5a in [HLK+12]: as we increase pre-strain p in the ribbon, the first unstable wavenumber q increases, meaning that the wavelength of the first unstable mode decreases. The dependence of wavelength on the width and thickness of the ribbon discussed in [HLK+12; LHS+14] can be accounted for by reverting to the unscaled set of variables using (2.13).

The predictions of the one-dimensional model concerning short-wavelength buckling are not very accurate, as revealed by the noticeable discrepancy between the black and red curves in Figure 4.1b. The green star is the prediction (4.6) of the critical point $(-\varepsilon^*, q^*)$ based on the one-dimensional model: comparison with the critical point produced by the full plate model (black curve) reveals that the critical wavenumber q^* is not accurately predicted. Dimensional reduction is based on the assumption that typical longitudinal scales are much larger than the ribbon width. This assumption is satisfied at the onset of the short-wavelength regime (near the bifurcation in the green curve in Figure 4.1c) but soon ceases to be valid deeper into the short-wavelength regime. More accurately, the prediction of the critical buckling wavenumber q^* near the transition to short-wavelength buckling relies on fourth-order corrections in the energy, which we do not calculate correctly here—by pushing the asymptotic expansion to fourth order, we could quantitatively predict how the critical wavenumber bifurcates from $q^* = 0$ at the onset of short-wavelength buckling. With the current second-order reduction, the one-dimensional model can only provide a qualitative picture of short-wavelength buckling.

4.3. Buckling diagram

The phase diagram in Figure 4.2 summarizes the results of the linear bifurcation analysis and shows the nature of the first critical mode as a function of the width-ratio parameter r and of the scaled pre-strain p , for a given Poisson's ratio $\nu = 0.5$. Different values of Poisson's ratio in the range $0 \leq \nu \leq 0.5$ lead to a similar diagram (data not shown).

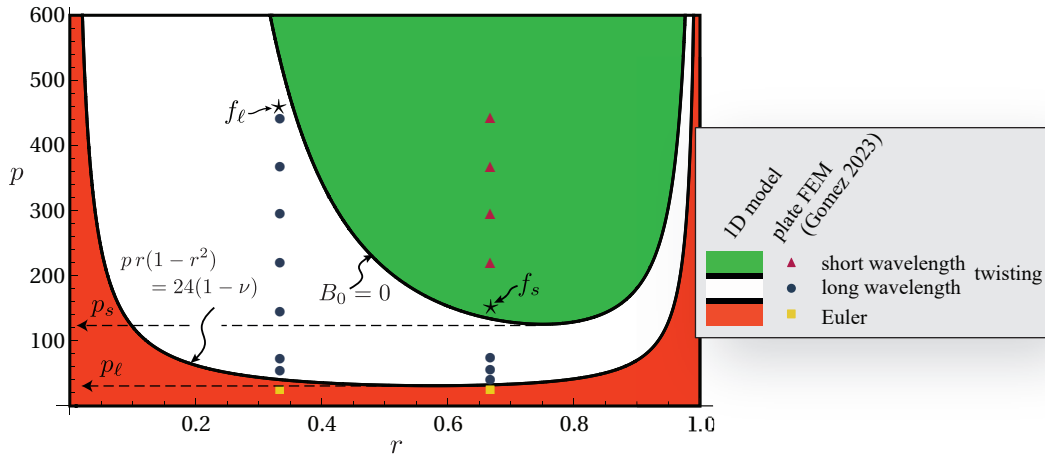


Figure 4.2. Phase diagram of an infinitely long ribbon having Poisson's ratio $\nu = 0.5$, as predicted by a linear bifurcation analysis of the one-dimensional model (background colors and black curves) and comparison to the 3D finite-element simulations reported in [GRA23] (symbols): the buckling pattern is shown in terms of the width ratio r and the scaled pre-strain p . The boundary between Euler (red) and long-wavelength twist buckling (white) is known from previous work [GRA23], see Equation (4.7). The boundary between long-wavelength (white) and short-wavelength (green) is novel and corresponds to a change of sign in the incremental gradient modulus B_0 . The ribbons with parameters corresponding to points f_ℓ and f_s are investigated in Section 5.

The boundary between the red domain (Euler buckling) and the white domain (long-wavelength twist buckling) has been identified in previous work [GRA23] based on the leading-order energy $\Phi^*|_{\nu^0}$. It can be found by equating the critical strain for Euler buckling, given by (3.3) as $\varepsilon_{\text{Euler}}^* = -pr$, and the critical strain for long-wavelength twist buckling, given by (4.6) as $\varepsilon_{\text{twist}}^* = -(pr^3 + 24(1-\nu))$. This yields

$$pr(1-r^2) = 24(1-\nu). \quad (4.7)$$

Euler buckling occurs first if $\varepsilon_{\text{Euler}}^* > \varepsilon_{\text{twist}}^*$, that is if $pr(1-r^2) < 24(1-\nu)$ (red region in the phase diagram).

By taking into account the gradient effect, the higher-order one-dimensional model proposed in this paper can also predict the transition from long- to short-wavelength twist buckling. Specifically, the analysis in Section 4.2 shows that the transition takes place along the curve with equation $B_0(p, r) = 0$, with $B_0(p, r)$ given in (2.29). This curve is included in the phase diagram in Figure 4.2 (upper solid curve). Short-wavelength twist buckling is expected to take place above this curve, something which we will confirm using a numerical post-buckling analysis of the one-dimensional model later in Section 5. The position of the boundary $B_0 = 0$ in the phase diagram agrees well with the 3D finite-element simulations reported in [GRA23] for $r = 1/3$ and $r = 2/3$ (symbols): in the finite-element simulations, a single perversion has been obtained whenever the condition $B_0 > 0$ holds (dark disks), whereas multiple perversions have been obtained whenever $B_0 < 0$ (red triangles).

In the phase diagram in Figure 4.2, the boundaries separating the orange, white, and green regions have a minimum each, implying that there exists two minimum values of the pre-strain, denoted as p_ℓ and p_s (for long- and short-wavelength instabilities, respectively), below which the ribbon cannot buckle, irrespective of the value of the width ratio $r \in [0, 1]$. The minimum pre-strain for long-wavelength buckling can be calculated as $p = 36\sqrt{3}(1-\nu)$ and occurs for $r = 1/\sqrt{3} = 0.578$. There is no simple closed-form expression of the coordinates of the minimum on the upper curve, but they can be found numerically as $p = 125.49$ and $r = 0.75$ for $\nu = 0.5$.

4.4. Weakly nonlinear solution for a perversion connecting two phases

In this section, we consider an infinite-length ribbon undergoing long-wavelength buckling, when $B_0 > 0$ (see Section 4.2). We derive a weakly non-linear solution representing a perversion connecting two semi-infinite helical domains (phases) having opposite chiralities, $\tau(S) = \pm\tau^*$. The perversion is the region across which the twisting strain $\tau(S)$ changes sign. In this region, the gradients $\tau'(S)$ cannot be neglected—the shape of the perversion is precisely determined by the gradient effect, as we show now. Non-linear expansions of the same kind have been derived for the analysis of bulging in cylindrical rubber balloons, see for instance [LA18; GWF22], and for the elasto-capillary buckling of soft cylinders, see for instance [LA20a; FJG21].

Without loss of generality, we assume that the perversion is centered around the origin $S = 0$ of the arc-length coordinate, in an infinite domain, $-\infty < S < +\infty$.

In this Section, we discard the fourth-order terms $\Phi^*|_{\gamma^4}$ discussed in Section 3.3, and give up on the positiveness of the energy. This amounts to dropping the second-gradient term in the energy density W in (2.27), which we replace with

$$\begin{aligned}\tilde{W}(p, r, \varepsilon; \tau, \tau') &= W(p, r, \varepsilon; \tau, \tau', \tau'' = 0) \\ &= \frac{1}{2} (A(p, r, \varepsilon; \tau) + B(p, r; \tau) \tau'^2).\end{aligned}\quad (4.8)$$

We derive the weakly nonlinear solution as a stationary point of the energy $\Phi^*|_{\gamma^0} + \Phi^*|_{\gamma^2} = \int_{-\infty}^{+\infty} \tilde{W} dS$ truncated at order γ^2 . Doing so we lose the positivity of the energy, and the stationary point we derive should not be expected to be a minimum, not even a local minimum. However, we can still expect that it is a good approximation to the minimum of the *positive* energy Φ^* , which differs by terms of order γ^4 only. This is all we require in the present Section.

As the strain energy \tilde{W} does not depend on the second gradient τ'' , the constitutive law (3.10) becomes

$$M(S) = \frac{\partial \tilde{W}}{\partial \tau} - \frac{d}{dS} \left(\frac{\partial \tilde{W}}{\partial \tau'} \right).\quad (4.9)$$

The balance of moments in (3.12) yields $dM/dS = 0$, *i.e.*, $M(S)$ is a constant.

Next, we observe that the Hamiltonian $H(S)$ defined by

$$\begin{aligned}H(S) &= \tilde{W} - \frac{\partial \tilde{W}}{\partial \tau'} \tau' - M \tau \\ &= \frac{1}{2} (A(p, r, \varepsilon; \tau) - B(p, r; \tau) \tau'^2) - M \tau\end{aligned}\quad (4.10)$$

is a conserved quantity, for any equilibrium solution such that $dM/dS = 0$. This classical results from Lagrangian mechanics can be established directly by calculating $dH/dS = 0$, assuming $dM/dS = 0$. With a small abuse of notation, we denote as H the constant value of $H(S)$.

Our two-phase solution connects two phases having opposite chiralities, *i.e.*, $\tau(S) \rightarrow \mp\tau^*$ for $S \rightarrow \pm\infty$. Taking the limit in (4.9), we get the constant value of the moment as $M(S) = \frac{\partial \tilde{W}}{\partial \tau}(\tau = \tau^*) = 0$. Next, taking the limit in (4.10), we find the value of Hamiltonian as $H = A(p, r, \varepsilon; \tau^*)/2$. We can therefore rewrite (4.10) as

$$B(p, r; \tau) \tau'^2 = A(p, r, \varepsilon; \tau) - A(p, r, \varepsilon; \tau^*),\quad (4.11)$$

for any S .

Focussing now on *weakly nonlinear buckling*, we assume that the buckling amplitude τ is small enough that we can approximate $B(p, r; \tau) \approx B(p, r; 0) = B_0(p, r)$, see (2.28)₂. Inserting the expression of $A(p, r, \varepsilon; \tau)$ given in (2.28)₁, and using $A_2 = -2A_4\tau^{*2}$ from (3.4), we get

$$\begin{aligned}B_0 \tau'^2 &= A_2 (\tau^2 - \tau^{*2}) + A_4 (\tau^4 - \tau^{*4}) \\ &= (\tau^2 - \tau^{*2}) (-2A_4 \tau^{*2} + A_4 (\tau^2 + \tau^{*2})) \\ &= A_4 (\tau^2 - \tau^{*2})^2\end{aligned}\quad (4.12)$$

Both sides of the equation are positive, as $B_0(p, r) > 0$ in the regime of long-wavelength buckling we study here: the signs are consistent. Separating the variables, taking the square root and integrating on both sides, we get

$$\int_0^{\tau(S)} \pm \frac{d\hat{\tau}}{\tau^{*2} - \hat{\tau}^2} = \sqrt{\frac{A_4}{B_0(p, r)}} \int_0^S d\hat{S}\quad (4.13)$$

where we have defined the center $S = 0$ of the perversion as the point where $\tau(0) = 0$.

The integral in the left-hand side of (4.13) is $\pm (\tau^*)^{-1} \tanh^{-1}(\tau(S)/\tau^*)$, and that in the right-hand side is S . Using successively (3.4), (2.29)₂ and (4.6), we can relate A_4 to the bifurcation parameter: $\tau^{*2} A_4 = -A_2/2 = -(24(1-\nu) + \varepsilon + pr^3)/24 = (\varepsilon^* - \varepsilon)/24$. This yields the weakly non-linear solution in the form

$$\tau(S) = -\tau^*(\varepsilon) \tanh \left(\sqrt{\frac{\varepsilon^* - \varepsilon}{24 B_0(p, r)}} S \right).\quad (4.14)$$

We have chosen the sign $\pm = -$, in such a way that we go from the phases having positive chirality to the phase having negative chirality when S increases, as in the upcoming Figure 5.2. In this figure, we compare the above prediction for $\tau(S)$ (with a shift in the origin $S \leftarrow S - \ell/2$ to adapt to the actual position of the perversion, dashed curves) to numerical results generated using the full one-dimensional model for a finite-length ribbon.

The width of the perversion, defined as the length of the interval of values of S such that $|\tau(S)/\tau^*| < 0.95$, is given from (4.14) by $2 \tanh^{-1}(.95) \sqrt{24 B_0(p, r) / (\varepsilon^* - \varepsilon)}$. It depends on the inverse square root of the bifurcation parameter $\varepsilon^* - \varepsilon \geq 0$, which points to the quick localization of perversions in the post-buckled regime (when ε becomes more negative than $\varepsilon^* < 0$). This localization of interfaces is classical in material instabilities, and is clearly visible in the simulations shown in Figure 5.2.

The weakly nonlinear analysis above assumes an infinitely long ribbon. It is applicable to a finite-length ribbon only as long as the perversion width predicted above is significantly smaller than the ribbon length, so that the perversion does not sense the boundaries. This excludes the very early stage of buckling.

5. SIMULATIONS OF FINITE-LENGTH RIBBONS IN THE POST-BUCKLING REGIME

This section presents numerical results for finite-length ribbons, both near the onset of buckling and far in the post-buckling regime. The simulations are based on the non-linear one-dimensional model (2.25). Specifically, we solve the boundary-value problem made up of the equilibrium equation (3.12), the higher-order constitutive law (3.10) and the boundary conditions (3.7) and (3.13), using the arc-length continuation method implemented in the Auto-07p library. The Auto-07p command files are distributed in the repository [KA24].

The analysis of finite-length ribbons in the post-buckled regime carried out in the present section complements the analysis of the infinite-length ribbon at the onset of instability from the previous section.

All post-buckling simulations use Poisson's ratio $\nu = 1/2$. The non-dimensional variables in (2.13) are calculated with the physical dimensions of ribbon $a = 18\text{mm}$ and $t = 2\text{mm}$. The other parameters vary and are specified later. In Subsection 5.1, the case of preferred long-wavelength buckling is considered (in the sense of the linear bifurcation analysis from Section 4, *i.e.*, with parameters such that $B_0 > 0$) and in Subsection 5.2 the case of preferred short-wavelength buckling is considered (for $B_0 < 0$). In both cases, we compare a nonlinear solution having a single perversion to one having 12-perversions—for the particular ribbon properties used in the simulations, these 12 perversions corresponds to the first critical wavenumber in the short-wavelength case. When $B_0 > 0$ (Subsection 5.1), we find that 1-perversion solutions are energetically favorable, while when $B_0 < 0$ (Subsection 5.2) 12-perversion solutions are favorable at least at the onset of buckling.

5.1. Case of preferred long-wavelength deformations

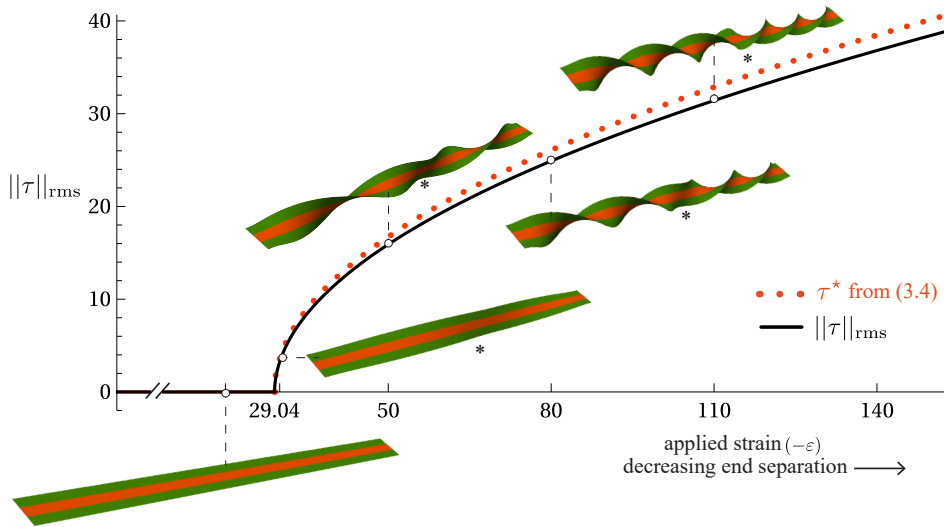


Figure 5.1. Bifurcation diagram: twist buckling of a finite-length ribbon whose short edges are progressively brought closer to one another (the quantity $-\varepsilon$ on the horizontal axis increases), as predicted by the one-dimensional model (black curve). Ribbon parameters are aspect-ratio $\ell = L/a = 300/18$, scaled pre-strain $p = 459.27$, and width ratio $r = 1/3$, corresponding to $B_0 = 0.018 > 0$ (preferred long-wavelength case, symbol f_ℓ in Figure 4.2). The prediction (3.4) ignoring the gradient effect is included for comparison (red dotted curve). We use the mean-square twist $\|\tau\|_{\text{rms}}$ as a measure of the buckling amplitude on the vertical axis, see (5.1). Three-dimensional views of the equilibrium configurations are included for specific values of the imposed axial strain: $-\varepsilon = 20$ (unbuckled), $-\varepsilon = (20, 30, 50, 80, 110)$. The onset of instability is at $-\varepsilon = 29.043$. In the buckling mode, the twist strain τ changes sign once in the middle of the ribbon, and this smooth feature evolves into a localized perversion in the post-buckled regime (star symbols).

In Figure 5.1, we simulate a finite-length ribbon having aspect-ratio $\ell = L/a = 300/18$, pre-strain $p = 459.27$ and

width-ratio $r = 1/3$: the linear bifurcation analysis from Section 4, applicable to the *infinite-length* case, predicts long-wavelength buckling as $B_0(p, r) = 0.018 > 0$ (given that the aspect-ratio $\ell = 300/18 \sim 15$ is quite large, one can expect that this prediction still holds).

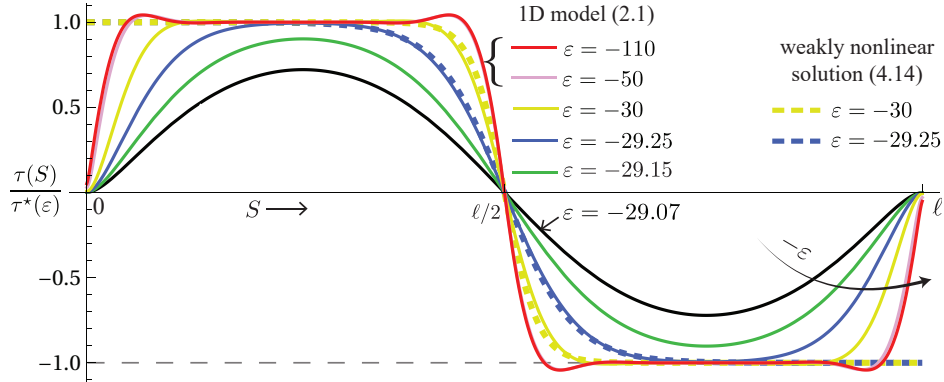


Figure 5.2. Formation of phases having uniform twisting strain $\tau(S) = \pm\tau^*(\varepsilon)$ in the post-buckled regime (plateaus in superimposed yellow, violet and red curves) by progressive localization from the initial sinus-like buckling mode (black, green, and blue curves). The plot shows the distribution of scaled twisting strain $\tau(S)/\tau^*(\varepsilon)$ along the centerline for applied strains $\varepsilon = -29.07, -29.15, -29.25, -30, -50$ and -110 . The 3D plots for the cases $\varepsilon = -30, -50, -110$ appear in Figure 5.1. The twisting strain $\tau(S)$ is scaled by the optimum value $\tau^*(\varepsilon)$ predicted by the leading-order model in (3.4). Note that the various curves are rescaled using *increasing* values $\tau^*(\varepsilon)$ as we go deeper into the post-buckling regime: unlike in Figure 3.1(a), the amplitudes in this plot do *not* convey the real buckling amplitude. By the clamping conditions in (3.7), the average of $\tau(S) = \theta'(S)$ over the length of the ribbon is always zero. The two dashed curves have been produced using the weakly nonlinear solution (4.14); the overlap with the corresponding solid curves confirms that the validity of the weakly nonlinear analysis.

We use the root mean square twist $\|\tau\|_{\text{rms}}$ to measure the amplitude of buckling in the bifurcation diagram,

$$\|\tau\|_{\text{rms}} = \left(\frac{1}{\ell} \int_0^\ell \tau^2(S) \, dS \right)^{\frac{1}{2}}. \quad (5.1)$$

This buckling amplitude is plotted in Figure 5.1 versus the scaled end-to-end shortening ($-\varepsilon$). The instability sets in at $-\varepsilon = 29.043$ in the simulations and the solution bifurcates into a solution that is invariant by mirror symmetry about the plane perpendicular to the axis passing through the midpoint $S = \ell/2$. The invariance by translation is lost, however. For all buckled solutions, starting with the small-amplitudes ones, the twisting strain $\tau(S)$ changes sign once at the midpoint $S = \ell/2$ (see the star symbol for $-\varepsilon = 30$ in Figure 5.1 and the curves in Figure 5.2).

As we progress along the bifurcated branch by reducing the end-to-end distance further, the twisting rate $\tau(S)$ tends to become uniform in both halves of the ribbon (helices having opposite chiralities in the 3D plots in Figure 5.1 for $-\varepsilon \geq 50$; plateaus in the red and violet overlapping curves in Figure 5.2) and a single perversion emerges as the gradient of twist localizes at the midpoint (star symbol in Figure 5.1; region of large gradient $\tau'(S)$ near $S = \ell/2$ in Figure 5.2). The evolution of this perversion in the post-buckled regime can be predicted by the weakly nonlinear analysis from Subsection 4.4. Indeed, in an intermediate range of values of ε including the green and blue curves in Figure 5.2, *i.e.*, when the two-phase solution is well formed (with τ plateauing at $\pm\tau^*$ in a significant fraction of the domain) and the interface between phases is still diffuse (it occupies a significant fraction of the domain), the assumptions of the weakly nonlinear analysis are satisfied and the hyperbolic-tangent solution (4.14) agrees well with the solutions of the one-dimensional model. Deeper in the post-buckled regime, for $-\varepsilon \geq 50$, the two phases having $\tau = \pm\tau^*$ are still present (horizontal dashed lines in Figure 5.2) but the interfaces develops an overshoot that is not captured by the weakly nonlinear solution (the overshoot can be seen in the superimposed red and violet curves in Figure 5.2). Overall, the phenomenon is highly reminiscent of phase separation [CGS85].

The small residual discrepancy on the value of $\|\tau\|_{\text{rms}}$ (from numerical simulations of the full one-dimensional model, black curve in Figure 5.1) and τ^* (from leading-order model, red dotted curve) can be attributed to the finite size of the boundary layers near the endpoints and at the perversion (steep regions near $S = \ell/2$ in Figure 5.2).

The bifurcation diagram in Figure 5.1 shows the first bifurcated branch only, but there are others, corresponding to larger wavenumbers at the onset of buckling. They give rise to a larger number of perversions. With n_p as number of perversions, the $n_p = 12$ branch is included in the buckling diagram in Figure 5.3(b). The branch bifurcates from the planar configuration at a slightly larger value $-\varepsilon^*(n_p = 12) = 31.148$ of the scaled end-to-end shortening than the single perversion, which has $-\varepsilon^*(n_p = 1) = 29.043$. This suggests that the solution with a single perversion (first buckling mode) is the one that connects with a stable section of the fundamental branch. This is consistent with the fact that the branch having a single perversion has everywhere lower energy than that having 12 perversions, see Figure 5.3(b). All these results point to the fact that the single-perversion solution is preferred. For a definitive

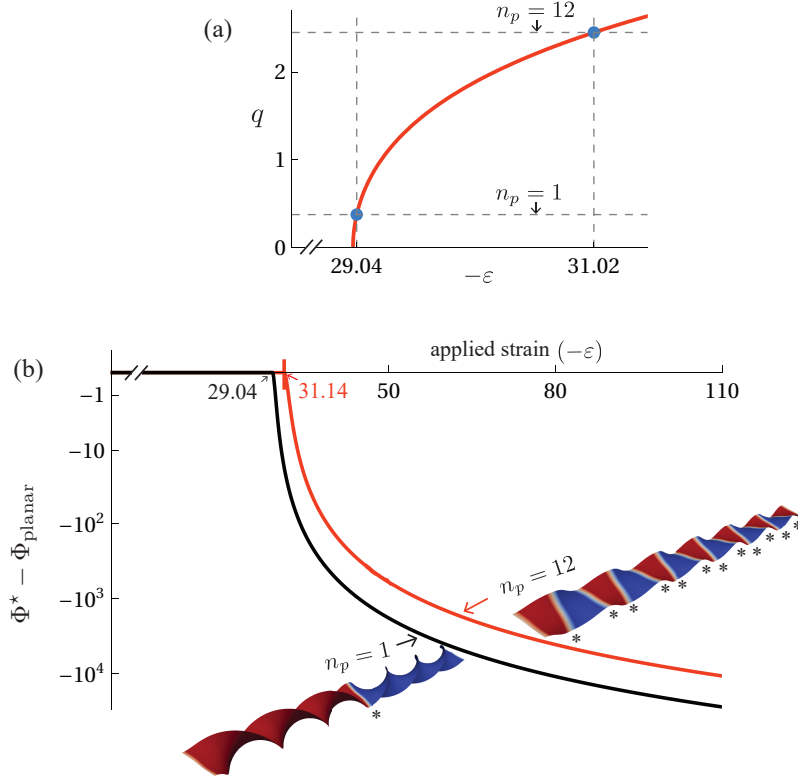


Figure 5.3. Comparison of the solution branches having a single perversion ($n_p = 1$) and 12 perversions ($n_p = 12$) in the preferred long-wavelength case. (a) Prediction of the critical scaled end-to-end shortening $-\varepsilon^*(n_p)$ as a function of n_p predicted by the dispersion relation $-\varepsilon^*(q)$ for an infinite ribbon with $q = \pi(n_p + 1)/\ell$, see Equations (4.5) and (5.2). (b) Bifurcation diagram showing the branches with $n_p = 1$ and $n_p = 12$ perversion(s). On the vertical axis, we show the difference in the energy Φ^* of the computed solution, as given by (2.25), and of the planar solution $\Phi_{\text{planar}} = \frac{1}{2}(\varepsilon^2 + rp(2\varepsilon + p))\ell$. For each branch, the mid-surface is plotted in 3D for $\varepsilon = -110$, and colored in red for $\tau < 0$, in white for $\tau \approx 0$ and in blue for $\tau > 0$.

statement, one could characterize the stability of the branches corresponding different number of perversions, something we have not undertaken.

Based on the infinitely-long ribbon calculations in Subsection 4.2, an accurate estimate of the critical end-to-end distance $-\varepsilon^*(n_p)$ as a function of the number of perversions n_p can be obtained by setting the wavenumber of the

mode as

$$q(n_p) = \pi \frac{n_p + 1}{\ell} \quad (5.2)$$

in the dispersion relation (4.5) derived in Section 4. This yields the estimates $-\varepsilon^*(n_p = 1) \approx 29.04$ and $-\varepsilon^*(n_p = 12) \approx 31.02$ obtained graphically in Figure 5.3(a), which provide accurate approximations to the critical loads $-\varepsilon^*(n_p = 1) = 29.04$ and $-\varepsilon^*(n_p = 12) = 31.14$ found in the nonlinear simulation in Figure 5.3(b). The approximation in (5.2) captures in a reasonably way the buckling modes produced by the simulations, which are approximately sinusoidal, see the case $n_p = 1$ in Figure 5.2 (black curve).

Remark 5.1. An additional complication arises with the sine-like approximation $\tau = \tau_0 \sin(q(n_p)S)$ underlying (5.2) when n_p is even, as the average of τ is then non-zero, in contradiction with the clamped boundary conditions (3.7). The numerical simulations suggest that for even values of n_p the incipient buckling mode is then a sine function having a *modulated amplitude*, whose wavenumber is still reasonably well approximated by (5.2). For more details on the amplitude modulation in $\tau(S)$, see the τ plot in the Mathematica file included as supplementary material [KA24].

To sum up, the post-buckling analysis shows that the solution having a single perversion ($n_p = 1$) is favored for a scaled pre-strain $p = 459.27$ and with ratio $r = 1/3$. This is consistent with the results of the *linearized* bifurcation analysis of an *infinitely long* ribbon in Section 4 (point f_ℓ in Figure 4.2).

5.2. Case of preferred short-wavelength deformations

In this section, we repeat the post-buckling analysis using this time a width ratio $r = 2/3$ and a pre-strain $p = 145.58$, corresponding to the symbol f_s in Figure 4.2. For these parameter values, the linear bifurcation analysis in Section 4 predicts short-wavelength buckling as $B_0 = -1.19 \times 10^{-2} < 0$. In the simulations, we switch to a larger aspect-ratio $\ell = L/a = 500/18$ to ensure that a significant number of perversions are included. The results are shown in Figure 5.4. The first bifurcation from the fundamental branch takes place at $-\varepsilon = 54.98$ and produces a solution having $n_p = 12$ perversions.

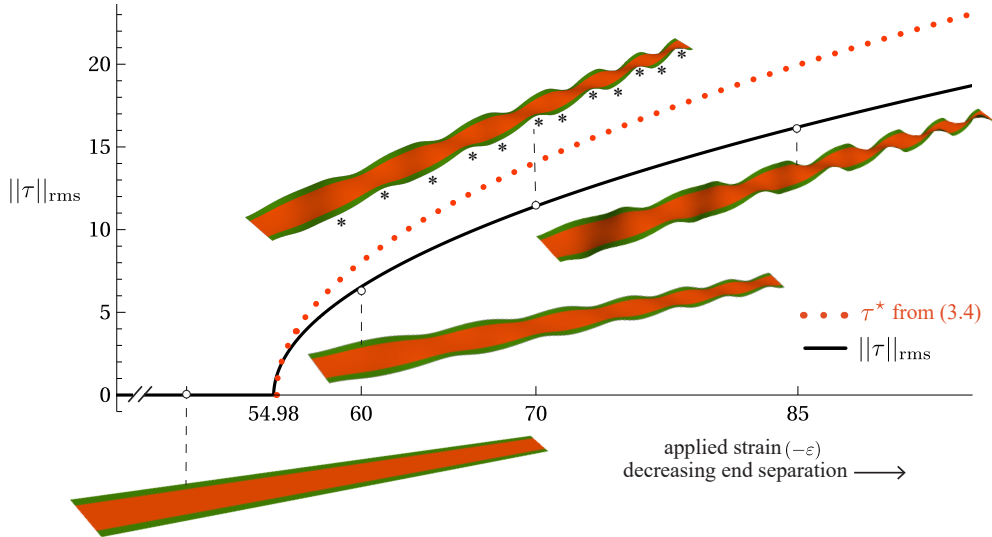


Figure 5.4. Bifurcation diagram showing the solution branch having $n_p = 12$ perversions that first bifurcates from the planar solution in the short-wavelength case. Simulation parameters are $\ell = 500/18$, $r = 2/3$ and $p = 145.58$, corresponding to the symbol f_s in Figure 4.2 (short-wavelength case). Same plot as in Figure 5.1, the 3D plots are produced for $-\varepsilon = 50$ (unbuckled) and $-\varepsilon = (60, 70, 85)$.

In Figure 5.4, the discrepancy between the root-mean-square value of the twist $\|\tau\|_{\text{rms}}$ from the nonlinear simulations (black curve) and the optimum value τ^* that ignores the gradient effect (dotted red curve) is significantly worse than in the long-wavelength case (Figure 5.1). Indeed, in the short-wavelength case, there are many perversions and they end up covering a significant fraction of the ribbon length. Thus, the plateaus in $\tau(S)$, which were visible earlier in Figure 5.2, have no longer enough room to form, even deep in the post-buckled regime (data not shown).

For $-\varepsilon = 60$, the twist-gradient terms amount to as much as 22.9% of the energy $\Phi^* - \Phi_{\text{planar}}$ that is released by buckling, and to an even larger fraction near the onset of buckling. This, together with the discrepancy seen in Figure 5.4, points to the fact that the size effects ignored by the leading-order model are no longer negligible.

In Figure 5.5(a), we repeat the argument from Section 5.1 that predicts the critical end-to-end shortening based on the dispersion relation (4.5). The critical strain from dispersion relations turns to be $-\varepsilon = 54.98$, which is very close to the critical value $-\varepsilon = 54.98$ observed in the non-linear simulations, see Figure 5.5(c,d). The dispersion relation can predict the number of perversions as well: equating q^* from (4.6) with the wavenumber $q(n_p)$ from (5.2), we calculate $n_p \approx 12$, in agreement with the non-linear simulations.

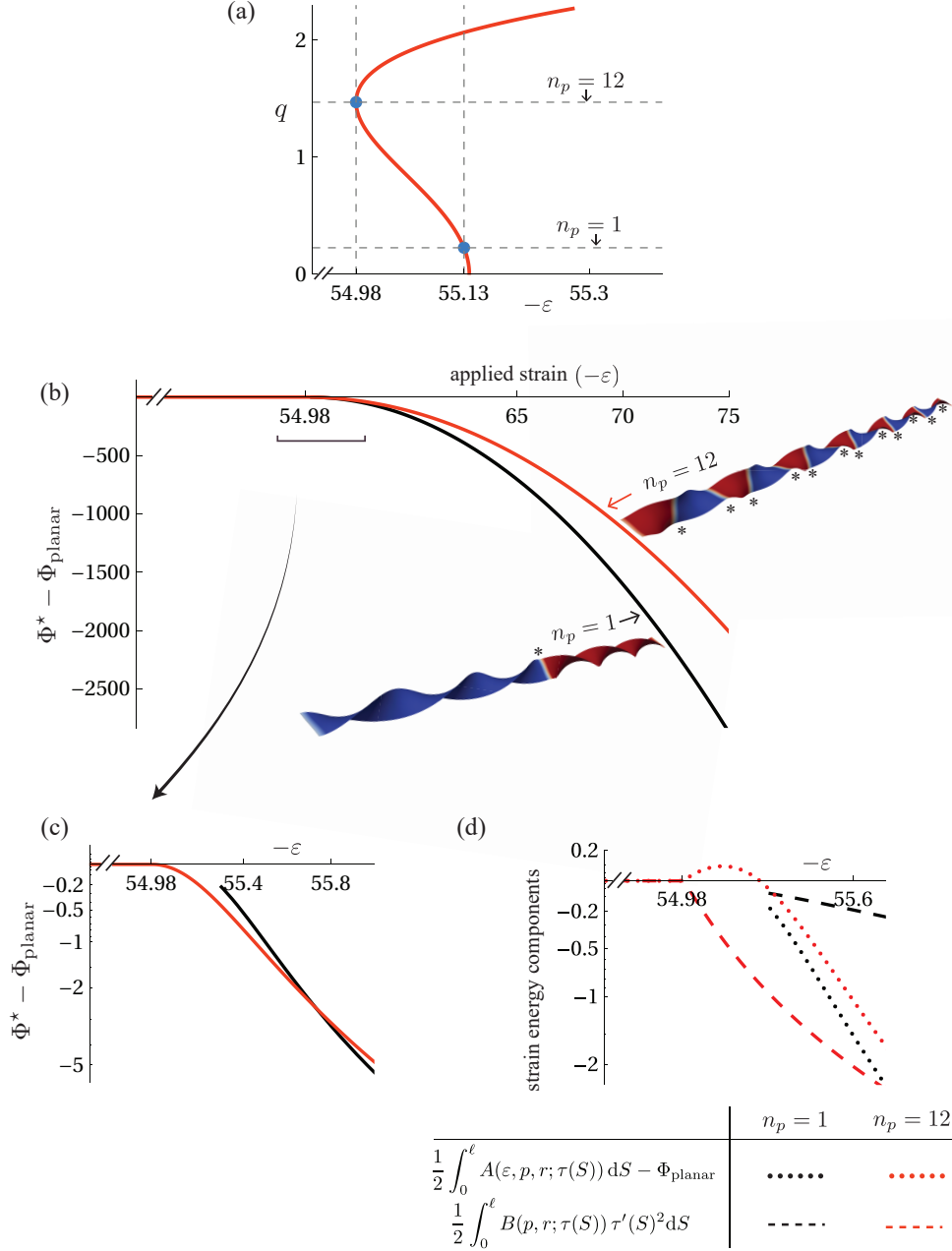


Figure 5.5. Comparison of the solution branches having a single perversion ($n_p = 1$) and 12 perversions ($n_p = 12$) in the preferred short-wavelength case. (a,b) Same plots as in Figure 5.3. (c) Close-up view near the onset of buckling. The energy of the solution is lower with $n_p = 12$ perversions (red curves) than with a single perversion ($n_p = 1$, black) immediately after buckling, up to $-\varepsilon < 55.7$, in agreement with the linear bifurcation analysis. Deeper in the post-buckled regime, the configuration with a single perversion becomes energetically favorable. (d) Breaking up the energy release associated with buckling into a leading-order contribution $\frac{1}{2} \int_0^\ell A(\tau) dS - \Phi_{\text{planar}}$ (dotted lines) and a contribution $\frac{1}{2} \int_0^\ell B(\tau) dS$ coming from the gradient τ' (dashed lines) reveals that the lower energy of the solution having $n_p = 12$ perversions, immediately above the buckling threshold, can be attributed to the gradient term, which is significantly more negative (red dashed curve). The leading-order terms, by contrast, remain comparable (dotted curves).

The competition between the solutions having $n_p = 1$ or $n_p = 12$ perversions is illustrated in Figure 5.5(b–d). Immediately above the buckling threshold, the solution with $n_p = 12$ is energetically favorable, as could be anticipated from the linear bifurcation analysis. In Figure 5.5(c), the difference is attributed to the energy contribution coming from the strain gradient: with $B_0 < 0$ (for the set of parameters chosen here), the more perversions there are, the more negative the twist-gradient contribution $\frac{1}{2} \int_0^\ell B(\tau) \tau'^2 dS \approx \frac{1}{2} \int_0^\ell B_0 \tau'^2 dS$ is.

On further decreasing the separation ends, the energy of the 1-perversion solution becomes lower than that of the 12-perversions solution, see Figure 5.5(d). The figure only shows the data for $n_p = 1$ and $n_p = 12$ and a similar cross-over is expected to take place with different numbers of perversions. In such conditions, we expect that there exist multiple stable equilibria in competition. Which one is obtained in experiments depends on multiple factors, including the details of the loading history.

To sum up, for $r = 2/3$ the short-wavelength twist buckling predicted in the phase diagram in Figure 4.2 has been confirmed in post-buckling simulations of ribbons having finite length. In this short-wavelength regime, the ribbon state with wavelength predicted by the linear bifurcation analysis has lowest energy early in the early post-buckled regime. Soon after, there are multiple equilibria in competition.

6. CONCLUDING REMARKS

We have presented in Section 2.6 a one-dimensional energy $\Phi^*[\tau]$ that captures the linear and non-linear features of twist buckling in pre-strained ribbons. The competition between short-wavelength and long-wavelength buckling has been shown to be governed by the sign of the gradient modulus $B_0(p, r)$, given in closed analytical form in Equation (2.29). This provides a simple answer to the question of wavelength selection and rationalizes the dependence of the buckling mode on experimental parameters (cross-section geometry, pre-strain level) reported in earlier work [LHS+14; HLK+12; LA17]. It is not surprising that shorter wavelengths are favored when $B_0 < 0$, as the energy cost associated with rapid variations of τ at perversions (gradient term $\frac{1}{2} \int B_0 \tau'^2 dS$) becomes *negative*. It is still surprising that the gradient term, which has been treated as a small correction in the dimension reduction procedure, plays a key role in the wavelength selection—upon reflection, this has to do with the fact that the leading-order model obtained in Equation (1.1) and in the previous work [GRA23] is degenerate—it cannot select a wavelength—, so that wavelength selection relies entirely on how the leading-order model is regularized.

To the best of our knowledge, this is the first time in the context of both higher-order homogenization and dimension reduction that a *negative* gradient modulus B_0 is connected to an observable behavior (namely, short-wavelength buckling) and not discarded as an undesirable mathematical oddity. This has been made possible by a novel truncation strategy, presented in Section 2.5, that keeps the dimensionally-reduced energy smooth, even when $B_0 < 0$ —see the *positivity* property discussed in Section 2.5, which in more accurate but technical terms is known as *lower semicontinuity*. Together, an improper truncation strategy used in earlier work (including ours) and a negative gradient modulus $B_0 < 0$ conspire to break this essential smoothness property and to make higher-order one-dimensional energies useless. We hope that our work clarifies the following important point: it is not necessarily the negative gradient modulus $B_0 < 0$ that must be blamed for the deficiencies of the dimensionally reduced/homogenized model, but the underlying truncation procedure.

Concretely, the naive truncation method from earlier work leads to two types of recurring issues: (i) the calculation of numerical solutions of the boundary-value equilibrium problem derived variationally from the one-dimensional energy fails due a lack of convergence, or (ii) it sometimes produces solutions having a strain energy lower than that of the stress-free state, which is contradictory. These difficulties disappeared immediately when we switched to the truncation procedure introduced in Section 2.5. In the future, it will be interesting to try to adapt this truncation procedure to other higher-order models produced by dimension reduction, as they display the same deficiencies. The new truncation procedure comes with a fee: as discussed in Sections 3.2 and 3.3, the highest-order terms in the energy are not the asymptotically correct ones, of the form $\int_0^\ell \frac{1}{2} B \tau'^2 dS$, but non-asymptotic ones, of the form $\int_0^\ell \frac{1}{2} (F \tau'^{r/2} + G \tau'^4) dS$, which are required to preserve positiveness. As a result, the equilibrium equation (3.12), when expressed in terms of the kinematic variable $\theta(S)$, is not just of order 4 but 6, see (2.14) and (4.2), which makes it more difficult to solve numerically—this issue is not really significant, however, in the one-dimensional setting studied here.

We proceed to discuss a few additional limitations of our approach. First, the reduction approach assumes that the twisting strain $\tau(S)$ evolves on a longitudinal length-scale much larger than the width a . This separation of scale is not satisfied around perversions, where $\tau(S)$ varies quickly, especially in the deep post-buckled regime: perversions may not be captured accurately by the one-dimensional model. We note that in the related problem of bulges propagating in cylindrical balloons [LA18], the same limitations apply in principle but the predictions of the dimensionally reduced model were still found to be highly accurate. Besides, the assumption on scale separation is not satisfied when buckling is short-wavelength (even early in the post-buckled regime), as the longitudinal wavelength then scales like the ribbon width. This limitation has been discussed at end of Section 4.2.

Another limitation of the one-dimensional model is that it involves cumbersome mathematical expressions, see Appendix B. In future work, we will explore variants of the truncation methods that preserve asymptotic correctness and positiveness of the energy while making the algebra simpler.

Although the one-dimensional model allows in principle the ribbon ends to rotate about the ribbon axis, we have not explored this possibility. We leave it to future work to investigate the new solutions and instabilities that result from the interplay between rotation and translations of the ends. By rotating the ends, it is in particular possible to create and remove perversions.

ACKNOWLEDGMENTS

Arun Kumar is supported by Marie Skłodowska-Curie (Europostdoc2) fellowship receiving funding from the European Union's Horizon 2020 research and innovation program under the Marie Skłodowska-Curie grant agreement no. 899987.

We gratefully acknowledge discussions with Claire Lestringant, Pedro M. Reis, and Michael Gomez. We are also grateful to an anonymous reviewer for suggesting to include the weakly nonlinear analysis for the two-phase solution.

This manuscript has been typeset using $\text{\TeX}_{\text{MACS}}$, a powerful, multi-platform and freely distributed scientific editor [vdHGG+13].

BIBLIOGRAPHY

- [22] Wolfram Research, Inc. Mathematica, Version 13.2. 2022. Champaign, IL, 2022.
- [AH16] B. Audoly and J. W. Hutchinson. Analysis of necking based on a one-dimensional model. *Journal of the Mechanics and Physics of Solids*, 97:68–91, 2016.
- [AL21] B. Audoly and C. Lestringant. Asymptotic derivation of high-order rod models from non-linear 3D elasticity. *Journal of the Mechanics and Physics of Solids*, 148:104264, 2021.
- [All69] H. G. Allen. *Analysis and Design of Structural Sandwich Panels*. Pergamon Press, New York, 1969.
- [AN21] B. Audoly and S. Neukirch. A one-dimensional model for elastic ribbons: a little stretching makes a big difference. *Journal of the Mechanics and Physics of Solids*, 153:104457, 2021.
- [Bak22] Harry Baker. How do octopuses change color? <https://www.livescience.com/how-do-octopuses-change-color>, 2022. [Accessed 05-04-2024].
- [BBE+98] Ned Bowden, Scott Brittain, Anthony G. Evans, John W. Hutchinson, and George M. Whitesides. Spontaneous formation of ordered structures in thin films of metals supported on an elastomeric polymer. *Nature*, 393(6681):146–149, 1998.
- [CGS85] J. Carr, M. E. Gurtin, and M. Slemrod. One-dimensional structured phase transformations under prescribed loads. *Journal of Elasticity*, 15:133–142, 1985.
- [CH11] Y. Cao and J. W. Hutchinson. From wrinkles to creases in elastomers: the instability and imperfection-sensitivity of wrinkling. *Proceedings of the Royal Society A: Mathematical, Physical and Engineering Sciences*, 468(2137):94–115, 2011.
- [DH05] G. Domokos and T. J. Healey. Multiple helical perversions of finite, intrinsically curved rods. *International Journal of Bifurcation and Chaos*, 15(3):871–890, 2005.
- [Eri75] J. L. Ericksen. Equilibrium of bars. *Journal of Elasticity*, 5(3–4):191–201, 1975.
- [FJG21] Y. Fu, Lishuai Jin, and A. Goriely. Necking, beading, and bulging in soft elastic cylinders. *Journal of the Mechanics and Physics of Solids*, 147:104250, 2021.
- [GRA23] Michael Gomez, Pedro M. Reis, and Basile Audoly. Twisting instabilities in elastic ribbons with inhomogeneous pre-stress: a macroscopic analog of thermodynamic phase transition. *Journal of the Mechanics and Physics of Solids*, 181:105420, 2023.
- [GWF22] Z. Guo, S. Wang, and Y. Fu. Localized bulging of an inflated rubber tube with fixed ends. *Philosophical Transactions of the Royal Society A: Mathematical, Physical and Engineering Sciences*, 380(2234), 2022.
- [HLK+12] Jiangshui Huang, Jia Liu, Benedikt Kroll, Katia Bertoldi, and David R Clarke. Spontaneous and deterministic three-dimensional curling of pre-strained elastomeric bi-strips. *Soft Matter*, 8(23):6291–6300, 2012.
- [HWQ+18] Changjin Huang, Zilu Wang, David Quinn, Subra Suresh, and K Jimmy Hsia. Differential growth and shape formation in plant organs. *Proceedings of the National Academy of Sciences*, 115(49):12359–12364, 2018.
- [KA24] A. Kumar and B. Audoly. Supplementary material for "wavelength selection in the twist buckling of pre-strained elastic ribbons". https://archive.softwareheritage.org/browse/origin/directory/?origin_url=https://github.com/arunkmaar/PrestrainedRibbons2024Paper, 2024. Accessed: 2024-08-18.
- [KAL23] A. Kumar, B. Audoly, and C. Lestringant. Asymptotic derivation of a higher-order one-dimensional model for tape springs. *Philosophical Transactions of the Royal Society A*, 381(2244):20220028, 2023.
- [KN05] Michael Kücken and Alan C Newell. Fingerprint formation. *Journal of theoretical biology*, 235(1):71–83, 2005.
- [Koi60] WT Koiter. A consistent first approximation in the general theory of thin elastic shells. *The theory of thin elastic shells*, pages 12–33, 1960.
- [LA17] Claire Lestringant and Basile Audoly. Elastic rods with incompatible strain: macroscopic versus microscopic buckling. *Journal of the Mechanics and Physics of Solids*, 103:40–71, 2017.
- [LA18] C. Lestringant and B. Audoly. A diffuse interface model for the analysis of propagating bulges in cylindrical balloons. *Proceedings of the Royal Society A: Mathematical, Physical and Engineering Sciences*, 474:20180333, 2018.
- [LA20a] C. Lestringant and B. Audoly. A one-dimensional model for elasto-capillary necking. *Proceedings of the Royal Society A*, 476(2240), 2020.
- [LA20b] C. Lestringant and B. Audoly. Asymptotically exact strain-gradient models for nonlinear slender elastic structures: a systematic derivation method. *Journal of the Mechanics and Physics of Solids*, 136:103730, 2020.
- [LHS+14] Jia Liu, Jiangshui Huang, Tianxiang Su, Katia Bertoldi, and David R Clarke. Structural transition from helices to hemi-helices. *PLoS one*, 9(4):1–7, 04 2014.
- [SKS+11] Thierry Savin, Natasza A Kurpios, Amy E Shyer, Patricia Florescu, Haiyi Liang, L Mahadevan, and Clifford J Tabin. On the growth and form of the gut. *Nature*, 476(7358):57–62, 2011.
- [TAL24] M. Thbaut, B. Audoly, and C. Lestringant. Effective boundary conditions for second-order homogenization. *Journal of the Mechanics and Physics of Solids*, page 105707, 2024.

- [vdHGG+13] J. van der Hoeven, A. Grozin, M. Gubinelli, G. Lecerf, F. Poulain, and D. Raux. GNU TEXmacs: a scientific editing platform. *ACM Communications in Computer Algebra*, 47(1–2):59–61, 2013.
- [YF23] X. Yu and Y. Fu. A one-dimensional model for axisymmetric deformations of an inflated hyperelastic tube of finite wall thickness. *Journal of the Mechanics and Physics of Solids*, 2023.

APPENDIX A. DEFICIENCIES OF THE PREVIOUS TRUNCATION METHOD

In Section 2.5, we proposed a novel truncation method, in which a second-order expansion of the optimal strain determined by dimension reduction is inserted into the shell energy, after which no additional truncation of the energy takes place. The energy produced by this procedure contains non-asymptotic fourth-order terms that warrant positiveness. In previous work, these fourth-order terms were discarded and we highlight in this Appendix the severe drawbacks associated with this truncation.

In this section, we work with the energy truncated beyond order ε^2 and consider loading conditions corresponding to a short-wavelength instability ($B_0 < 0$, green region in the phase diagram in Figure 4.2). We show that the truncated energy can be made infinitely large and negative when small-amplitude, short-wavelength twisting perturbations are included on top of the planar configuration. This shows that the energy functional is unbounded from below, in a small ‘neighborhood’ around the planar configuration.

By way of illustration, we use the loading and material parameters $p = 400$, $\nu = 1/2$, $r = 2/3$ and $\varepsilon = -10$. The parameters fall inside the green region in phase diagram in Figure 4.2 and give $B_0 = -0.50$. For a given ribbon length ℓ , we pick a large integer $n \gg q \gg 1$ and consider the following configuration

$$\theta(S) = \frac{1}{q} \sin(qS), \quad (\text{A.1})$$

where

$$q = \frac{2\pi n}{\ell}. \quad (\text{A.2})$$

For $n \gg q \gg 1$, this is a small-amplitude, short-wavelength perturbation on top of the planar configuration, as announced. The kinematic boundary conditions (3.7) are satisfied, so it makes sense to evaluate the energy of this configuration. The twisting strain is given by $\tau(S) = \cos(qS)$.

- The boundary contributions to the energy can be written as

$$[W_b(p, r; \tau, \tau')]_0^\ell = [C(p, r; \tau) \tau \tau']_0^\ell. \quad (\text{A.3})$$

They vanish, as $\tau'(S) = q \sin(qS) = 0$ at both $S = 0$ and $S = \ell = 2\pi n/q$.

- The truncated strain energy per unit length is given, on average, as

$$\begin{aligned} \frac{1}{\ell} (\Phi^*|_{\gamma^0} + \Phi^*|_{\gamma^2}) &= \frac{q}{2n\pi} \int_0^{2\pi n/q} \frac{1}{2} (A(p, r, \varepsilon; \tau) + B(p, r; \tau)) dS \\ &= \frac{21034257523}{414720} - \frac{31657868810803 q^2}{251418359808000} \end{aligned} \quad (\text{A.4})$$

This average strain energy decreases without limit when the wavenumber q increases. As a result, small amplitude, short-wavelength ribbon configurations can have a negative energy. This is contradictory as the completely relaxed, ribbon state shown in Figure 2.1(a) has zero energy.

APPENDIX B. DETAILED EXPRESSIONS OF THE HOMOGENIZED CONSTANTS

In this Appendix, we provide the detailed expressions of the second and fourth order terms entering into the one-dimensional strain energy density, as obtained in the companion Mathematica notebook. We note that the somewhat cumbersome fourth-order terms are not asymptotically exact. The coefficients are listed below and can also be output from the supplementary Mathematica file when required.

The coefficients entering the strain energy terms at second-order are

$$\begin{aligned} B_2 &= \frac{1}{1512 \cdot 10^2} \left[-(38 + 75\nu) + \frac{1}{192} p r^3 (5r^6 - 27r^4 + 63r^2 - 41) \right] \\ B_4 &= -\frac{1}{399168 \cdot 10^3} \\ C_0 &= \frac{1}{210} \left[(4 - 11\nu)(1 - \nu) - \frac{1}{96} p r (1 - r^2) (155\nu - 12(1 - \nu)r^4 + (9 - 93\nu)r^2 + 83) \right. \\ &\quad \left. - \frac{1}{192} p^2 r^4 (1 - r)^3 (12r - r^2(r + 3) + 4) \right] \\ C_2 &= \frac{1}{302400} \left[34 + 67\nu - \frac{1}{256} p r (15r^8 - 84r^6 + 210r^4 - 164r^2 + 23) \right] \\ C_4 &= \frac{1}{199584 \cdot 10^3}. \end{aligned}$$

The coefficients at fourth order are

$$\begin{aligned}
F_2 &= \frac{1}{(1-\nu^2) 18162144 \cdot 10^3} \left[F_{20} + \frac{1}{384} p r^3 (1-r^2) F_{21} + \frac{1}{512} p^2 r^6 F_{22} \right] \\
F_{20} &= 38688 \nu^4 - 53352 \nu^3 + 601431 \nu^2 + 742432 \nu + 175304 \\
F_4 &= \frac{1}{(1-\nu^2) 163459296 \cdot 10^4} \times \left[239 \nu^3 - 239 \nu^2 + 2706 \nu + 1833 - \right. \\
&\quad \left. \frac{p r^3 (1-r^2)}{12288} (105 r^{10} - 1785 r^8 + 18690 r^6 - 98570 r^4 + 255589 r^2 - 378317) \right] \\
F_6 &= \frac{211}{(1-\nu^2) 66691392768 \cdot 10^5} \\
G_0 &= \frac{1}{(1-\nu^2) 11346799464 \cdot 10^4} \left[G_{00} - \frac{1}{3072} p r^3 (1-r^2) G_{01} + \frac{1}{36864} p^2 r^6 (1-r)^2 G_{02} \right. \\
&\quad \left. + \frac{1}{294912} p^3 r^9 (1-r)^3 G_{03} + \frac{3}{8388608} p^4 r^{12} (1-r)^4 G_{04} \right] \\
G_{00} &= 4106878205 \nu^4 - 2881076420 \nu^3 + 3541082920 \nu^2 + 939320762 \nu + 311567294 \\
G_2 &= G_{20} - \frac{p r^3 (1-r^2)}{196608} G_{21} - \frac{p^2 r^6 (1-r)^2}{786432} G_{22} - \frac{p^3 r^9 (1-r)^3}{4194304} G_{23} \\
G_{20} &= 2354948525 \nu^3 - 2100214260 \nu^2 + 425446473 \nu - 423403490 \\
G_4 &= \frac{1}{2235228720012288 (1-\nu^2) \cdot 10^6} \left(G_{40} + \frac{p r^3 (1-r^2)}{8192} G_{41} + \frac{p^2 r^6 (1-r)^2}{131072} G_{42} \right) \\
G_{40} &= 2642285920 \nu^2 - 2026907108 \nu + 383369127 \\
G_6 &= \frac{1}{462692345042543616 (1-\nu^2) \cdot 10^7} \left(408799133 \nu - 120028728 + \frac{3}{524288} p r^3 G_{61} \right) \\
G_8 &= \frac{1242599}{5552308140510523392 (1-\nu^2) \cdot 10^8} \\
H_0 &= \frac{1}{190702512 (1-\nu^2) \cdot 10^3} \left(H_{00} + \frac{p r^3 (1-r^2)}{3072} H_{01} + \frac{p^2 r^6 (1-r)^2}{73728} H_{02} + \frac{p^3 r^9 (1-r)^3 \nu}{294912} H_{03} \right) \\
H_{00} &= 932138 \nu^4 - 276512 \nu^3 + 2294332 \nu^2 + 2716787 \nu + 520436 \\
H_2 &= \frac{1}{233419874688 (1-\nu^2) \cdot 10^4} \left(H_{20} + \frac{p r^3 (1-r^2)}{12288} H_{21} + \frac{p^2 r^6 (1-r)^2}{98304} \nu H_{22} \right) \\
H_{20} &= 2460858 \nu^3 + 139473 \nu^2 + 2990527 \nu + 2170322 \\
H_4 &= \frac{1}{45616912653312 (1-\nu^2) \cdot 10^5} \left(281828 \nu^2 + 97754 \nu + 156351 + \frac{p r^3 (1-r^2) \nu}{131072} H_{41} \right) \\
H_6 &= \frac{9733 \nu}{11495461988634624 (1-\nu^2) \cdot 10^6}
\end{aligned}$$

$$F_{21} = \begin{pmatrix} 1 \\ r^2 \\ r^4 \\ r^6 \\ r^8 \end{pmatrix}^T \begin{pmatrix} 2484827 & 3055877 & -543153 & 543153 \\ -1340995 & -1839013 & 237627 & -237627 \\ 344975 & 521345 & -53235 & 53235 \\ -21105 & -33495 & 6825 & -6825 \\ -630 & 630 & 0 & 0 \end{pmatrix} \begin{pmatrix} 1 \\ \nu \\ \nu^2 \\ \nu^3 \end{pmatrix};$$

$$G_{03} = \begin{pmatrix} 1 \\ r \\ r^2 \\ r^3 \\ r^4 \\ r^5 \\ r^6 \\ r^7 \\ r^8 \\ r^9 \\ r^{10} \\ r^{11} \end{pmatrix}^T \begin{pmatrix} -14966919369 & 42652592454 \\ -44900758107 & 127957777362 \\ 31294397466 & -18733023312 \\ -53235239850 & 148077142432 \\ -11519696070 & -52162839294 \\ 79251916806 & -154499024490 \\ -13694135184 & 36474234022 \\ -22424496840 & 33815219442 \\ 4460899959 & -6168481296 \\ 2367903213 & -2937096992 \\ -309190770 & 309190770 \\ -103063590 & 103063590 \end{pmatrix} \begin{pmatrix} 1 \\ \nu \end{pmatrix};$$

$$H_{01} = \begin{pmatrix} 1 \\ r^2 \\ r^4 \\ r^6 \\ r^8 \\ r^{10} \end{pmatrix}^T \begin{pmatrix} 100981034 & 124562071 & 3457614 & 128863879 \\ -57727516 & -93929657 & 8711772 & 26576239 \\ 16542680 & 35265370 & -597450 & -47687990 \\ -1455300 & -4694550 & -3780630 & 12892530 \\ -22050 & 177135 & 1114260 & -1269345 \\ 0 & 36015 & -72030 & 36015 \end{pmatrix} \begin{pmatrix} 1 \\ \nu \\ \nu^2 \\ \nu^3 \end{pmatrix};$$

$$\begin{aligned}
H_{21} &= \begin{pmatrix} 1 \\ r^2 \\ r^4 \\ r^6 \\ r^8 \\ r^{10} \\ r^{12} \end{pmatrix}^T \begin{pmatrix} 405177507 & 213140601 & 659829952 \\ -273735819 & 187436244 & 493276243 \\ 105568470 & -213733275 & -754858895 \\ -20016990 & 75470640 & 381621450 \\ 1911735 & -10503885 & -99464610 \\ -112455 & -1448580 & 12856515 \\ 0 & 513135 & -513135 \end{pmatrix} \begin{pmatrix} 1 \\ \nu \\ \nu^2 \end{pmatrix}; \\
H_{02} &= \begin{pmatrix} 1 \\ r \\ r^2 \\ r^3 \\ r^4 \\ r^5 \\ r^6 \\ r^7 \\ r^8 \\ r^9 \\ r^{10} \end{pmatrix}^T \begin{pmatrix} 16651530 & 3487957 & 17847679 \\ 33303060 & 6975914 & 35695358 \\ -7432740 & 110314713 & 253998201 \\ -48168540 & -52212088 & -24194956 \\ -75600 & -30105518 & -216174908 \\ 48017340 & 23450652 & 689940 \\ -25871580 & -16642734 & 78367740 \\ 1845900 & -5880 & -6806940 \\ 922950 & 5078745 & -8485155 \\ 0 & -561750 & 561750 \\ 0 & -280875 & 280875 \end{pmatrix} \begin{pmatrix} 1 \\ \nu \\ \nu^2 \end{pmatrix}; \\
G_{01} &= \begin{pmatrix} 1 \\ r^2 \\ r^4 \\ r^6 \\ r^8 \\ r^{10} \\ r^{12} \end{pmatrix}^T \begin{pmatrix} -37056466835 & -440865665917 & 551744017305 & -928871364565 \\ 43959053632 & 208396376414 & -121451262900 & 44743988810 \\ -19086355715 & -86478631435 & 89361711075 & 39042719975 \\ -1921392900 & 54346488000 & -109600627500 & 59335917900 \\ 3914084475 & -24357330375 & 40931947875 & -20488701975 \\ -1125211500 & 4777698450 & -6179762400 & 2527275450 \\ 114604875 & -343814625 & 343814625 & -114604875 \end{pmatrix} \begin{pmatrix} 1 \\ \nu \\ \nu^2 \\ \nu^3 \end{pmatrix}; \\
(G_{21}; H_{41}) &= \begin{pmatrix} 1 \\ r^2 \\ r^4 \\ r^6 \\ r^8 \\ r^{10} \\ r^{12} \\ r^{14} \end{pmatrix}^T \left(\begin{pmatrix} -4282442995193 & 18678820465282 & -31380035648345 \\ 1615791655423 & -3646723160894 & 4895166992815 \\ -1102085913005 & 3516905287210 & -3468342996125 \\ 1559496090075 & -6833414052150 & 7505562946875 \\ -1205695944075 & 4736914071750 & -4529781542475 \\ 502338068925 & -1677807013050 & 1349496305325 \\ -111510543375 & 301438471950 & -189927928575 \\ 10429043625 & -20858087250 & 10429043625 \end{pmatrix} \begin{pmatrix} 1 \\ \nu \\ \nu^2 \end{pmatrix}; \begin{pmatrix} 270678919 \\ 375726271 \\ -753317645 \\ 586163355 \\ -255694155 \\ 67913085 \\ -10362735 \\ 779625 \end{pmatrix} \right); \\
G_{41} &= \begin{pmatrix} 1 \\ r^2 \\ r^4 \\ r^6 \\ r^8 \\ r^{10} \\ r^{12} \\ r^{14} \\ r^{16} \end{pmatrix}^T \begin{pmatrix} -345591960729 & 1130500161659 \\ 114401942346 & -224306992888 \\ -157467666930 & 261006696020 \\ 291841373250 & -589895376000 \\ -271979561700 & 523095553050 \\ 149046335550 & -260020450200 \\ -49875313950 & 76368190500 \\ 9601341750 & -12428262000 \\ -827701875 & 827701875 \end{pmatrix} \begin{pmatrix} 1 \\ \nu \end{pmatrix}; \quad G_{61} = \begin{pmatrix} 1 \\ r^2 \\ r^4 \\ r^6 \\ r^8 \\ r^{10} \\ r^{12} \\ r^{14} \\ r^{16} \\ r^{18} \\ r^{20} \end{pmatrix}^T \begin{pmatrix} 1788369267803 \\ -2489202835658 \\ 1792168200075 \\ -3256263530520 \\ 4522599504150 \\ -3955998217500 \\ 2308238959950 \\ -914519251800 \\ 239868003375 \\ -38074286250 \\ 2814186375 \end{pmatrix}; \\
(G_{02}; H_{22}) &= \begin{pmatrix} 1 \\ r \\ r^2 \\ r^3 \\ r^4 \\ r^5 \\ r^6 \\ r^7 \\ r^8 \\ r^9 \\ r^{10} \\ r^{11} \\ r^{12} \end{pmatrix}^T \left(\begin{pmatrix} 56080803699 & -176546411266 & 312740176130 \\ 112161607398 & -353092822532 & 625480352260 \\ -6325529499 & 136497711228 & 353107968855 \\ -58099219596 & 6465240988 & -165500404550 \\ 18299360322 & -211033659700 & -43447028620 \\ 2071005840 & 102434967612 & -78110940690 \\ -41791663350 & 215595739176 & -186658072170 \\ 13216103460 & -59168257260 & 51198179550 \\ 19585590255 & -70219706130 & 53257128750 \\ -4272826950 & 12519313800 & -8246486850 \\ -3661700175 & 9310230300 & -5648530125 \\ 450084600 & -900169200 & 450084600 \\ 225042300 & -450084600 & 225042300 \end{pmatrix} \begin{pmatrix} 1 \\ \nu \\ \nu^2 \end{pmatrix}; \begin{pmatrix} 8427907 \\ 16855814 \\ 213305268 \\ 96641922 \\ -395355057 \\ -75486436 \\ 287111872 \\ -429660 \\ -88682895 \\ 5390910 \\ 14143500 \\ -1305990 \\ -652995 \end{pmatrix} \right);
\end{aligned}$$

$$G_{22} = \begin{pmatrix} 1 \\ r \\ r^2 \\ r^3 \\ r^4 \\ r^5 \\ r^6 \\ r^7 \\ r^8 \\ r^9 \\ r^{10} \\ r^{11} \\ r^{12} \\ r^{13} \\ r^{14} \end{pmatrix}^T \begin{pmatrix} 981678423081 & -3010525867061 \\ 1963356846162 & -6021051734122 \\ -548040698397 & -720676924587 \\ -259719721356 & 1548221436948 \\ 1623146721249 & -2893968378165 \\ -784142087346 & 1344229595522 \\ -2421064585773 & 5500409459581 \\ 855726643800 & -1651333697160 \\ 1420292646675 & -2828256962055 \\ -392685952050 & 673939376250 \\ -446408034975 & 738407805975 \\ 91092122100 & -128940065100 \\ 72289282275 & -91213253775 \\ -8747477550 & 8747477550 \\ -4373738775 & 4373738775 \end{pmatrix} \begin{pmatrix} 1 \\ \nu \end{pmatrix}; \quad G_{42} = \begin{pmatrix} 1 \\ r \\ r^2 \\ r^3 \\ r^4 \\ r^5 \\ r^6 \\ r^7 \\ r^8 \\ r^9 \\ r^{10} \\ r^{11} \\ r^{12} \\ r^{13} \\ r^{14} \\ r^{15} \\ r^{16} \end{pmatrix}^T \begin{pmatrix} 255331900357 \\ 510663800714 \\ -214006240113 \\ -69066740140 \\ 564542538517 \\ -259552867626 \\ -904075547793 \\ 351477437640 \\ 666083203695 \\ -217807439850 \\ -291973117275 \\ 77277885300 \\ 77632041375 \\ -15364682550 \\ -11488435875 \\ 1352458800 \\ 676229400 \end{pmatrix}$$

$$(F_{22}, G_{04}, G_{23}, H_{03}) = \begin{pmatrix} 1 \\ r \\ r^2 \\ r^3 \\ r^4 \\ r^5 \\ r^6 \\ r^7 \\ r^8 \\ r^9 \\ r^{10} \\ r^{11} \\ r^{12} \\ r^{13} \end{pmatrix}^T \begin{pmatrix} 26431 & 4360025503 & -181956550249 & -403647 \\ 0 & 17440102012 & -545869650747 & -1210941 \\ -91091 & -36665388722 & 516977012578 & 11543160 \\ 0 & 82409090252 & -726374589074 & 12233056 \\ 140998 & -66643705279 & -291552964707 & -43423998 \\ 0 & 3230350072 & 1278917648879 & 27154398 \\ -193622 & 10914067460 & -165805724820 & -1235504 \\ 161280 & -1474516360 & -569033268204 & -2553384 \\ -45461 & -680302319 & 117172111713 & 226677 \\ 0 & 63744652 & 130315694931 & 75559 \\ 1465 & 16920718 & -27612876270 & 0 \\ 0 & 787644 & -13767265890 & 0 \\ 0 & 196911 & 1876084875 & 0 \\ 0 & 0 & 625361625 & 0 \end{pmatrix};$$